TÉCNICO LISBOA

Improvement of state-resolved kinetic models applied to N_2-CH_4 hypersonic entry flows

João Francisco da Cruz Vargas

Thesis to obtain the Master of Science Degree in

Engineering Physics

Supervisors:

Jorge Manuel Amaro Henriques Loureiro

Mário António Prazeres Lino da Silva

Examination Committe

Chairperson: Prof. Luís Paulo da Mota Capitão Lemos Alves

Supervisor: Prof. Mário António Prazeres Lino da Silva

Member of the committe: Prof. David Pacheco Resendes

October 2015

"That's one small step for a man..." - Neil Armstrong

Acknowledgments

I would like to acknowledge my advisors contributions to this work, Prof. Jorge Loureiro and Prof. Mário Lino da Silva whose counseling have guided and pointed me in the right direction. This work wouldn't exist without them. I would also like to extend my sincere thanks to Dr. Bruno Lopez invaluable help with navigating the SPARK code, advice on Fortran programming and all around critic and counselor. Thanks also to Prof. Vasco Guerra which provided me with already treated data of the cross section of the collision $N_2 + e^-$. Besides these people who have helped me directly, there is also all those who have aided me indirectly. Friends, colleagues and family, to them I would also like to extend my acknowledgments.

Resumo

Apesar de terem sido aplicados com sucesso na entrada da sonda Huygens em Titã em 2004, os modelos para esta atmosfera não são fisicamente consistentes para altas temperaturas. Desenvolvimentos na área permitiram a criação de um modelo que não violasse a consistência física. Neste trabalho, propomos algumas adições e modificações a este modelo, extendê-lo para cinética de estado-para-estado e aplicá-lo à radiação emitida por um gás num tubo de choque para diferentes velocidades da onda de choque. Este tratamento permite comparações com resultados experimentais do tubo de choque X2. Descobrimos que os resultados estão em acordo para baixas velocidades de choque mas apesar de uma pequena melhoria para altas velocidades, os resultados não estão em acordo com a experiência.

Palavras-chave: Entrada atmosférica, Titã, estado-para-estado, radiação do plasma, tubo de choque.

Abstract

Previous kinetic models for Titan's atmosphere, although successfully employed in the Huygens probe entry in 2004, are not physically consistent for high temperature flows. New developments have allowed to create a model which doesn't violate physical consistency. In this work, we propose some additions and modifications to this model to extend it for state-to-state kinetics and apply it to compute the radiation emitted by a shock-tube flow for different shock wave speeds. These treatment allows for comparison with experimental results from the X2 shock-tube. It is found that there is reasonable agreement with the experiments for low speeds and while there is some improvement for higher speeds, the results are not in agreement with the experiments.

Keywords: Atmospheric entry, Titan, state-to-state, plasma radiation, shock-tube.

Contents

List of Figures

List of Tables

Abbreviations

ESS - Electronic State Specific

VSS - Vibrational State Specific

FHO - Forced Harmonic Oscillator

HO - Harmonic Oscillator

Spark - Software Package for Aerothermodynamics Radiation and Kinetics

VT - Vibrational - Translational

VD - Vibrational - Dissociation

Nomenclature

$\boldsymbol{u}$ velocity vector

ΔE_{nm} Energy difference between vibrational levels n and m of a certain species

$\dot{\Omega}$ Energy sink term

$\dot{\omega}_i$ Mass source term

ϵ_i Internal energy of species i.

γ Specific heat ratio

$\mathcal{R}$ Universal gas constant

μ Reduced mass

ν Stoichiometric coefficient

ρ Total gas density

σ Reaction cross section

θ Third Arrhenius coefficient

θ_{rot} Characteristic Rotational temperature

A First Arrhenius coefficient

A^* Equivalent Einstein coefficient

A_0 Rotational spectroscopic constant of a species

A_{nm} Einstein coefficient of a certain species between vibrational levels n and m

B_0 Rotational spectroscopic constant of a species

C_0 Rotational spectroscopic constant of a species

c_2 Second radiation constant

c_i Mass fraction of species i

C_v Specific heat capacity at constant volume

E Internal energy of the gas in chapter 2 or energy of the system in chapter 3

g_i Specific Gibbs free energy of species i

g_s Degeneracy of energy level s

H Enthalpy of the gas

I Radiation intensity

k Boltzmann constant

$k_{\mathrm{b},r}$ Backward reaction rate constant

K_{e} Equilibrium constant

$k_{\mathrm{f},r}$ Forward reaction rate constant

M_i Molar mass of species i

M_z Mach number of the flow

n Second Arrhenius coefficient

N_i Number density of species i

P_0 Atmospheric pressure

p_z Gas pressure

Q_i^m Partition function of energetic mode m and species i

r_i Specific gas constant

T Temperature of the gas

u_z Gas velocity

x_i Molar concentration of species i

z Index, upstream of the shock $z = 1$ or post-shock $z = 2$

1 Introduction

A spacecraft enters the upper layers of a planetary atmosphere at hypersonic speeds of several km/s. These may typically range from about 6 km/s when entering from orbit (such as a space shuttle returning from the International Space Station) to about 12 km/s when returning from outer space (hyperbolic trajectories). At such high speeds, a strong shock wave is formed upstream of the spacecraft, dramatically decreasing the flow speed, whose coherent energy is transformed in thermal agitation energy, leading to post-shock temperatures of several tens of thousand of kelvins.

These strong heating processes lead to the dissociation and ionization of the gas and a so-called entry plasma is formed between the shockwave and the spacecraft forebody. The understanding and appropriate modeling of the physical-chemical properties of such a plasma is key to the design of a spacecraft, namely of its thermal protections.

1.1 State-to-state kinetics

In equilibrium, gases follow a Boltzmann distribution. Atmospheric entry flows are completely in non-equilibrium. This implies that it is not correct to assume an equilibrium distribution on the gas in post-shock. The corollary is that an accurate description of the gas in a post-shock relaxation phase can only be achieved by modeling the population of the individual levels of species. This is called state-to-state or state-specific: to model individually the population of each energy level in a species and account for the interactions with the other components of the gas on a state-by-state basis. In state-to-state kinetics, each energy level is treated as a *pseudo*-species having it's own mass conservation equation.

To associate the electronic levels of species to it's own mass conservation equation is equivalent to treat each level as an independent species. This is called Electronic State Specific (ESS) model. The same can be done with vibrational the levels by associating a mass conservation equation to each vibrational level of a given electronic level of a molecule. This is called Vibrational State Specific (VSS) model. These two types of models are used within this work. The next step would be to track down the rotational levels of molecules, this would be Rotational State Specific (RSS) model, but this is beyond the scope of this work.

1.2 Motivation and objectives

In 1997, the Cassini-Huygens spacecraft was launched from Earth for an interplanetary voyage to Saturn. Arriving in 2004, the Huygens probe detached from the spacecraft and successfully entered the atmosphere of Titan, composed of 98% N_2 and 2% CH_4 mixture. It was the first time a spacecraft landed on an outer Solar System object. Before this, several studies were carried out in order to study the entry point of the spacecraft at 5.15 km/s. It was feared that the highly radiative characteristics of CN, previously unaccounted for, would lead to excessive heating of the spacecraft during descent. At this time, models were developed and created around the 5.15 km/s entry point. The result was Gökçen's kinetic scheme [5] which was deployed in the

aerothermal database of the Huygens spacecraft.

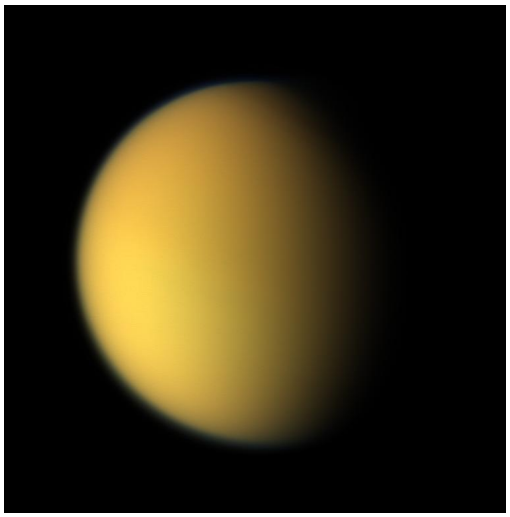

Figure 1: Real color photo of Titan. Credit: NASA.

It was later verified by Lino da Silva *et al.* that not all the rates in the kinetic scheme developed by Gökçen were physically consistent for high temperatures [9]. A new physically consistent kinetic scheme was then proposed by the same authors. Since there is still interest in future missions to Titan, experiments in shock tube facilities of N_2-CH_4 mixtures are still being performed as recently as in 2009 [7]. It is then our objective to put this new kinetic model to the test by comparing it with the older model, and to apply these to the modeling of the most recent experimental results available. However before doing this , some changes needed to be made to our in-house thermodynamical and kinetic models. The objectives of this work are then twofold:

- To improve and assess the influence of changes introduced into the thermodynamical and kinetic models of IST's aerothermodynamics code Spark,
- To compare the modified Gökçen and Lino da Silva kinetic models and to apply the results to the simulation of post-shock radiation in a shock tube.

The modifications we are introducing to both kinetic schemes are of a state-specific nature in order to produce meaningful comparisons between models and the experimental results. Our main tool to achieve this objective is the Spark code, the in-house code of aerothermodynamics of IST. Also used extensively is the Gas and Plasma Radiation database (GASPAR) available at the European shock tube for high enthalpy research (ESTHER).

1.3 Structure

This thesis is divided in three main parts. First we start by describing in chapter 2 the theoretical framework of this thesis. In chapter 3 we introduce, discuss and assess changes in the kinetic and thermodynamical

models established in the previous chapter. Chapter 4 presents the comparison and analysis of both Gökçen and Lino da Silva models as well as the comparison with the experimental results from A. Brandis [7]. We conclude this work in chapter 5 presenting the perspectives for future developments of this aerothermal model.

2 Theory and models

2.1 Hydrodynamics

Neglecting transport phenomena, the system of governing equations is formed by the mass and the total energy conservation equations [2]:

$$\frac{\partial}{\partial t}\begin{bmatrix}\rho c_i \\ \rho E\end{bmatrix} + \boldsymbol{\nabla}\cdot\begin{bmatrix}\rho \boldsymbol{u} c_i \\ \rho \boldsymbol{u} H\end{bmatrix} = \begin{bmatrix}\dot{\omega}_i \\ \dot{\Omega}\end{bmatrix} \tag{1}$$

In the first equation, ρ denotes the gas density, c_i the mass fraction of species i, $\boldsymbol{u}$ the velocity vector, $\dot{\omega}_i$ the mass source term. In the second equation, E is the internal energy of the gas, H the enthalpy and $\dot{\Omega}$ the energy sink of the system. A temporal relaxation sub-system is extracted from the full set of conservative equations (1) by neglecting the spatial derivatives and setting the gas velocity to zero [2]:

$$\frac{\partial}{\partial t}\begin{bmatrix}\rho c_i \\ \rho E\end{bmatrix} = \begin{bmatrix}\dot{\omega}_i \\ \dot{\Omega}\end{bmatrix} \quad \Longrightarrow \quad \frac{\partial}{\partial t}\begin{bmatrix}c_i \\ T\end{bmatrix} = \frac{1}{\rho}\begin{bmatrix}\dot{\omega}_i \\ \left(\dot{\Omega} - \sum \varepsilon_i \dot{\omega}_i\right)/C_{\mathrm{V}}\end{bmatrix} \tag{2}$$

The LHS system in (2) can be formulated in term of primitive variables (mass fractions and temperature), leading to the system in the right hand side in which C_v is the constant volume heat capacity and ϵ_i the internal energy of species i. The derivation of this system is done on appendix A. Such a zero-dimensional system allows the study of thermo-chemical relaxation processes occurring in a gas which is suddenly heated to a given temperature keeping the pressure constant. Note that this situation is similar to a re-entry flow in which the upstream gas is suddenly heated to very high temperatures as it crosses the shock wave. As a result, this temporal system represents a very powerful, yet simple, set of equations to study the relaxation processes occurring in complex atmospheric entry flows. Depending on the thermo-kinetic model considered for each chemical species, the mass conservation equations are associated to either chemical species or to an internal level, either electronic or vibronic.

The system (2) represents a set of Ordinary Differential Equations (ODE) which is integrated with a time marching technique using the DVODE library [22]. In order to close the system, a set of initial conditions need to be defined. Any gas state can be used as initial conditions and the system (2) will then be integrated until equilibrium is reached. However, in order to maintain a close analogy with the flow behind normal shock waves, the initial conditions are set to some post-shock conditions, which are computed from an upstream gas state using the Rankine-Hugoniot jump relations. Assuming frozen gas composition, the Rankine-Hugoniot

jump relations are [1]:

$$\begin{cases} \dfrac{\rho_2}{\rho_1} = \dfrac{M_1^2\left(\gamma+1\right)}{2+M_1^2\left(\gamma-1\right)} \\ \dfrac{u_2}{u_1} = \dfrac{2+M_1^2\left(\gamma-1\right)}{M_1^2\left(\gamma+1\right)} = \left(\dfrac{\rho_2}{\rho_1}\right)^{-1} \\ \dfrac{p_2}{p_1} = 1+\dfrac{2\gamma}{\gamma+1}\left(M_1^2-1\right) \\ \dfrac{T_2}{T_1} = \dfrac{\left(2\gamma M_1^2-(\gamma-1)\right)\,\left(2+(\gamma-1)\,M_1^2\right)}{M_1^2\left(\gamma+1\right)^2} \end{cases} \tag{3}$$

where index 1 and 2 refer to the upstream and the post-shock conditions respectively, M_1 is the upstream Mach number and $\gamma = C_p/C_v$ is the specific heat ratio.

2.2 Kinetics

The mass source term reads [1]:

$$\dot{\omega}_i = M_i \sum_r \Delta\nu_{ir}\left[k_{\mathrm{f},r}\prod_i x_i^{\nu'_{ir}} - k_{\mathrm{b},r}\prod_i x_i^{\nu''_{ir}}\right] \tag{4}$$

where ν'_{ir} and ν''_{ir} are the reactant and product stoichiometric coefficients, $\Delta\nu_{ir} = \nu''_{ir} - \nu'_{ir}$ and $x_i = \rho_i/M_i$ is the molar concentration of species i and M_i it's molar mass. The rate constants $k_{\mathrm{f},r}$ and $k_{\mathrm{b},r}$ are associated to the forward and backward processes of the r reaction and are a function of temperature only.

In this work the $k_{\mathrm{f},r}$ are expressed either through the Arrhenius function or a 9th order polynomial. The Arrhenius function is given by [1]

$$k_{\mathrm{f},r}(T) = AT^n \exp\left(-\theta/kT\right), \tag{5}$$

and the 9th order polynomial by [10]

$$k_f(\tilde{T}) = \exp\left(\sum_{k=-3}^{4} c_k \tilde{T}^k + c_5 \log\tilde{T}\right), \tag{6}$$

where $\tilde{T} = T/1000$ and T in kelvin. By knowing either the Arrhenius coefficients or the polynomial coefficients, the forward rate can be determined as a function of temperature only.

The backward rate is computed from detailed balancing using the equilibrium constant $K_{\mathrm{e}}(T)$:

$$k_{\mathrm{b}}(T) = \frac{k_{\mathrm{f}}(T)}{K_{\mathrm{e}}(T)} \tag{7}$$

which imposes physical consistency between k_{f} and k_{b}. The equilibrium constants are computed through the Gibbs free energies or through the partition functions. Using the species' Gibbs free energies K_{e} is given by [1]:

$$K_{\mathrm{e}} = \exp\left[-\sum_i^{N_s}\Delta\nu_{ir}\frac{g_i}{r_i T}\right]\left(\frac{P_0}{\mathcal{R}\,T}\right)^{\sum_i^{N_s}\Delta\nu_{ir}} \tag{8}$$

where P_0 is the atmospheric pressure, $\mathcal{R}$ is the universal gas constant and $r_i = \mathcal{R}/M_i$ are the specific gas constants, M_i being the molar mass of species i. The Gibbs free energies are computed using analytic expressions based on the separation of internal energy modes. When using the partition functions K_e reads:

$$K_\mathrm{e} = \prod_i^{N_s} \left(Q^\mathrm{tot}\right)^{\Delta\nu_{ir}}, \tag{9}$$

where the total partition is the product of the translational and the internal partition functions:

$$Q^\mathrm{tot} = Q_\mathrm{trans} \times Q_\mathrm{int}. \tag{10}$$

2.3 Thermodynamics

When studying microscopic phenomena, such as radiation and Vibrational-Translational (V-T) relaxation, it is important to account for the internal states of species. In equilibrium, a species follows a Boltzmann distribution of it's internal levels. As a consequence the chemical species are treated with only one mass conservation equation. In non-equilibrium no distribution can be assumed *a priori*. The occupation levels of each species must then be individually tracked to distinguish between the species states. This is carried out in a so-called state-to-state kinetic approach with a different mass conservation equation for each internal level.

If the electronic levels are allowed to depart from the Boltzmann distribution function then a new mass conservation equation associated to each electronic level is added to the system. The kinetic and radiative processes are now related to the electronic levels and not the chemical species. Notice that the vibrational levels of each molecule are still following the Boltzmann distribution at a given temperature. Relaxing this assumption, each vibronic state needs to be individually described by a mass conservation equation. The collisional and radiative processes now involve the vibrational levels. The rotational levels of a molecule are still following a Boltzmann distribution. The next step would be to relax this assumption and create a kinetic scheme which allows for rotational interactions. This is not done here as it is outside the scope of this work.

The nomenclature utilized throughout this work is as follows: a Boltzmann simulation accounts only for the flow chemical species following a Boltzmann distribution, an electronic state specific (ESS) accounts for some molecular species electronic levels and a vibrational state specific simulation (VSS) accounts for the vibronic states of some chemical species (specifically, only N_2 which accounts for most of the gas composition).

2.3.1 Partition function

The internal partition function of a species has contributions from its three different modes: rotation, vibration and electronic. Generically, the partition function of a mode is computed through

$$Q \equiv \sum_s Q_s \equiv \sum_s g_s \exp\left(-\beta\epsilon_s\right), \tag{11}$$

where $\beta = 1/kT$, s is the number of energy levels in the mode, g_s the degeneracy of each level and ϵ_s the energy of level s. The exact computation of this partition function may be carried out using an extensive

database detailing the degeneracy and energy of the levels of each mode. If possible or necessary, the partition function calculation can be replaced with an approximated model, as sometimes it is expensive to compute it analytically. At other times there is no *a priori* knowledge on the energy levels of the modes.

The rotational partition function is computed differently depending on the configuration of the molecule. Θ_{rot} is a constant called the rotational temperature and the product of the second radiation constant $c_2 = hc/k$ and a constant dependent on the species B_v. For a diatomic molecule, if $\Theta_{\text{rot}} << T$ the rotational partition function is simply [27]

$$Q^{\text{tot}}_{\text{rot},i} = \sum_s Q_{\text{rot},is} \approx \frac{T}{\sigma\Theta_{\text{rot}}}, \tag{12}$$

where σ is a symmetry factor with value 1 for non-symmetric molecules and 2 for symmetric molecules. For linear poly-atomic molecules the rotational partition function is [25]

$$Q^{\text{tot}}_{\text{rot},i} = \sum_s Q_{\text{rot},is} = \frac{T}{\sigma\Theta_{\text{rot}}} \exp\left[\frac{1}{3}\left(\frac{\Theta_{\text{rot}}}{T}\right) + \frac{1}{90}\left(\frac{\Theta_{\text{rot}}}{T}\right)^2\right]. \tag{13}$$

For non-linear poly-atomic molecules [25],

$$Q^{\text{tot}}_{\text{rot},i} = \sum_s Q_{\text{rot},is} = \frac{1}{\sigma}\sqrt{\pi\left(\frac{T}{c_2}\right)^3\left(\frac{1}{A_0B_0C_0}\right)}, \tag{14}$$

where $c_2 = hc/k$ is the second radiation constant and A_0, B_0 and C_0 are constants related to the rotational moments of inertia that depend on the species.

In SPARK code, the vibrational partition function can be computed either from a set of tabulated vibrational levels, which requires a database or considering the harmonic oscillator approximation. From the quantum harmonic oscillator, the energy of vibrational level v is given by $\epsilon_v = \hbar\omega_e(v+1/2)$ and the degeneracy is $g_v = 1$. ω_e is a spectroscopic constant that depends on the specie. The vibrational partition function is then approximated to a geometric series, yielding [1]

$$Q^{\text{tot}}_{\text{vib},i} = \sum_s Q_{\text{vib},is} = \frac{1}{1 - \exp\left(-\frac{\hbar\omega_e}{kT}\right)}. \tag{15}$$

Note that this model is inadequate to use with VSS simulations since these require the expressions for the individual partition functions Q_{vib}. Further analysis of this model and comparison with an exact computation of the vibrational partition function is done in section 3.2.

The electronic partition function can only be computed through the electronic energy levels and the definition (11). Then, for a Boltzmann species the internal partition function is given by

$$Q^{\text{tot}}_{\text{int},i} = Q^{\text{tot}}_{\text{rot},i} \times \left[\sum_v Q_{\text{vib},iv}\right] \times \left[\sum_e Q_{\text{ele},ie}\right]. \tag{16}$$

For an ESS species, the total partition function is the sum of the individual partition functions of a species in one particular energy level e',

$$Q^{\text{tot}}_{\text{int},i} = Q^{\text{tot}}_{\text{rot},i} \times \left[\sum_v Q_{\text{vib},iv}\right] \times Q_{\text{ele},i}. \tag{17}$$

A VSS species must have it's electronic and vibrational energy levels specified, e' and v'. The total partition function is accordingly given by:

$$Q^{\text{tot}}_{\text{int},i} = Q^{\text{tot}}_{\text{rot},i} \times Q_{\text{vib},i} \times Q_{\text{ele},i}. \tag{18}$$

The translational mode contribution is computed based on the close proximity of adjacent translational energy levels by approximating the sum of the levels to an integral [1] yielding [1],

$$Q_{\text{trans}} = \left(\frac{2\pi mkT}{h^2}\right)^{3/2} V. \tag{19}$$

The full partition function can then be known.

2.3.2 Gibbs free energy

The Gibbs free energies of a specie are computed through the Born-Oppenheimer approximation, separating the contribution of each energy mode of the specie

$$g_i^{\text{total}} = g_i^{\text{trans}} + g_i^{\text{ele}} + g^{\text{vib}} + g_i^{\text{rot}}. \tag{20}$$

Each contribution depends on the partition function associated to that energy mode by

$$g_i^m = -r_i T \log Q_i^m, \tag{21}$$

where Q_i^m is the partition function of mode m and species i.

2.4 Radiation

The energy sink term in system (2) exists only because of radiation. For the typical times of a shock tube experiment, no other heat transfer process can occur that accounts any significant energy exchange. As such, assuming an optically thin gas, the radiated intensity is computed through [8]

$$I_{\text{rad}} = \sum_{i,j} N_i \times A_{ij} \times \Delta E_{ij}, \tag{22}$$

where N_i is the number density, A_{ij} is the Einstein coefficient of the transition and ΔE_{ij} the energy difference between the higher and lower energy levels. Here, i is the index of the excited (higher) level and j the ground (lower) level. The total energy sink is then,

$$\dot{\Omega} = -I_{\text{rad}}. \tag{23}$$

The Einstein coefficients and the energy differences are known for each different transition. Only transitions of ESS species are considered for equation (22) since the radiative processes in this application suppose electronic excitation and de-excitation.

[1] since the energy spacings are low enough to assume the range of possible energies is no longer discrete.

3 Theoretical model improvement

This section details the author contribution to the theoretical framework and modeling of N_2-CH_4 shocked flows. In subsection 3.1 we detail how N_2 dissociation by electronic impact was determined and included in Lino da Silva's kinetic scheme. Subsection 3.2 details the comparison of two different models for the vibrational partition function. Subsection 3.3 details the spontaneous emission modeling contributions and subsection 3.4 details the vibrational redistribution of rates for VSS simulations.

3.1 Nitrogen dissociation by electron impact

The forward rate of reaction

$$N_2 + e^- \rightleftarrows 2N + e^- \tag{24}$$

was computed in this work. Due to the large concentrations of N_2 in the flow, we should not neglect reactions that can directly impact the population of this species. As this rate was missing from Lino da Silva's kinetic [9], a rate must either be computed from cross section data or an alternative rate must be found in the literature. For an arbitrary dependence of the cross section σ on energy E, the reaction rate can be computed through [4]

$$k(T) = \frac{1}{kT}\left(\frac{8}{\pi\mu kT}\right)^{1/2}\int_0^\infty E \times \sigma(E) \times \exp\left(-E/kT\right) dE, \tag{25}$$

where μ is the reduced mass of the colliding particles. The cross section data from [18] is used in (25). The integration of (25) leads to tabulated values of k_f as a function of temperature. These values are then fitted using an Arrhenius function. The resulting Arrhenius function coefficients can then be directly used in SPARK code.

In figure 2 we find the fitted rate and the data computed through (25) and in table 1 the results of the fitted coefficients. These results were fitted in a $T = 300 - 100000$ K range which allows us to cover the low and high temperature conditions. The agreement between the fitting and the results is good.

Table 1: Fitting results of the forward rate $N_2 + e^-$ to an Arrhenius function

	A (m^3/mol/s)	n	θ (K)
Fit results	7.892×10^{15}	-1.479	1.154×10^5

In figure 3 the fitted rate obtained in this thesis and literature rates are plotted. The hard-sphere limit is also plotted as a physical ceiling to this reaction. The other rates are taken from Park, Laporta and Sarrette respectively [24, 17, 21]. Notice that we are searching for the rate which gives us more confidence to be used with Lino da Silva kinetics. Sarrette's rate is non-physical for higher temperatures and therefore cannot be used in our model. The three other rates remain as possible choices for Lino da Silva kinetics. Park's rate becomes flat over 50000 K. This suggests that electron impact dissociation is as much important at 50000

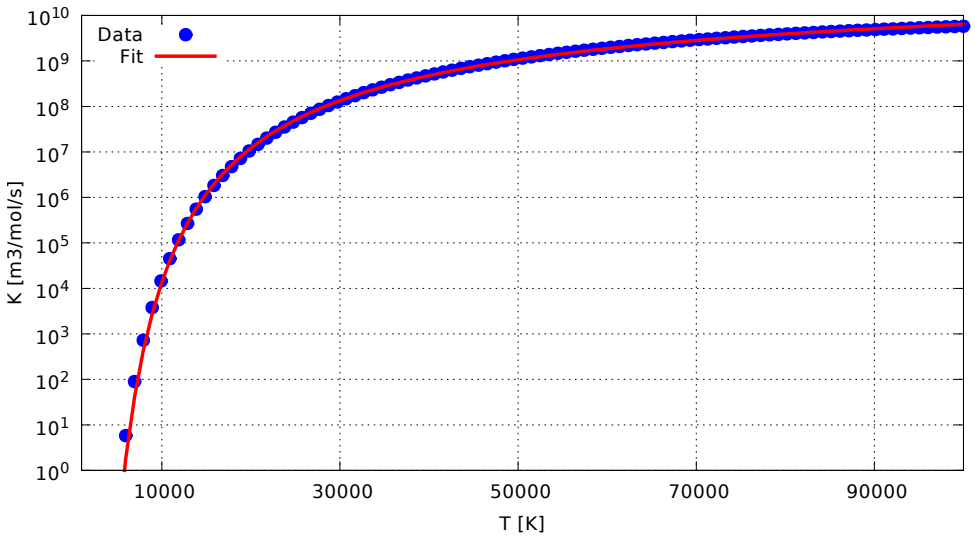

Figure 2: Fitted forward reaction rates for $N_2 + e^-$ and computed data.

K as at 100000 K. The same situation happens with Laporta's rate with the exception that this rate is estimated as being two orders of magnitude lower. Intuitively, for higher temperatures, electrons have more translational energy and thus, can contribute to dissociation more efficiently. This effect should not cap and as such, the rate we computed seems more acceptable to be used in Lino da Silva's kinetic. Alternatively, it is possible that electron impact dissociation proceeds preferentially from excited states at high temperatures, hence explaining the low values of Laporta rate. In any case, Park's rate has been successfully utilized in the computation of hypersonic plasma flows [23] and the cross-section we used for determining our new rate has also been successfully applied to the modeling of non-equilibrium low temperature plasmas which gives us confidence in this choice for our model.

To assess the impact of this rate or it's absence we have simulated Lino da Silva's original kinetic with and without N_2 dissociation by electron impact. The impact is very small and can only be seen slightly in figure 4 through the molar fraction of N_2. This implies that the presence of this rate in the kinetic scheme is not very meaningful for the simulations we are doing. This rate may drag the computational time up and really hold no impact whatsoever but it is included for the sake of completeness.

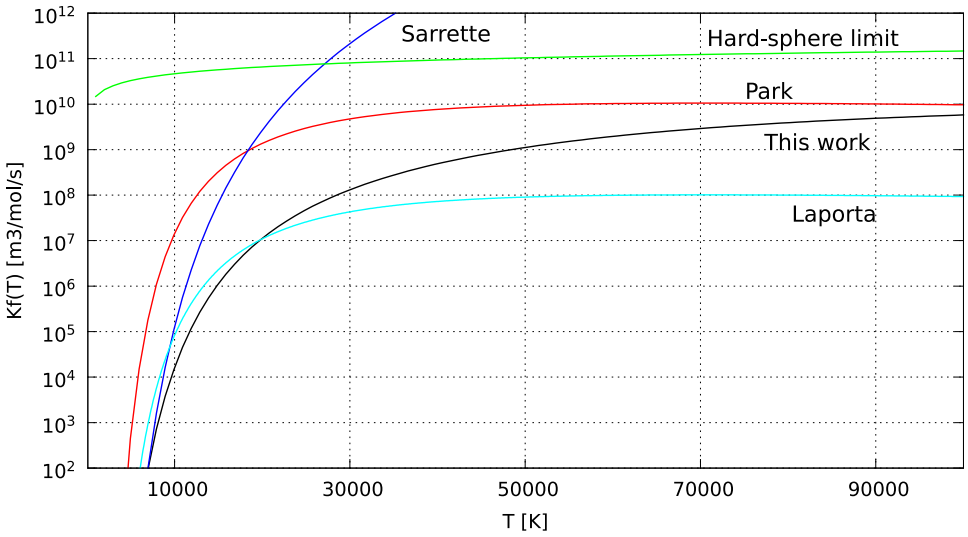

Figure 3: Forward reaction rates for N_2 dissociation by electronic impact.

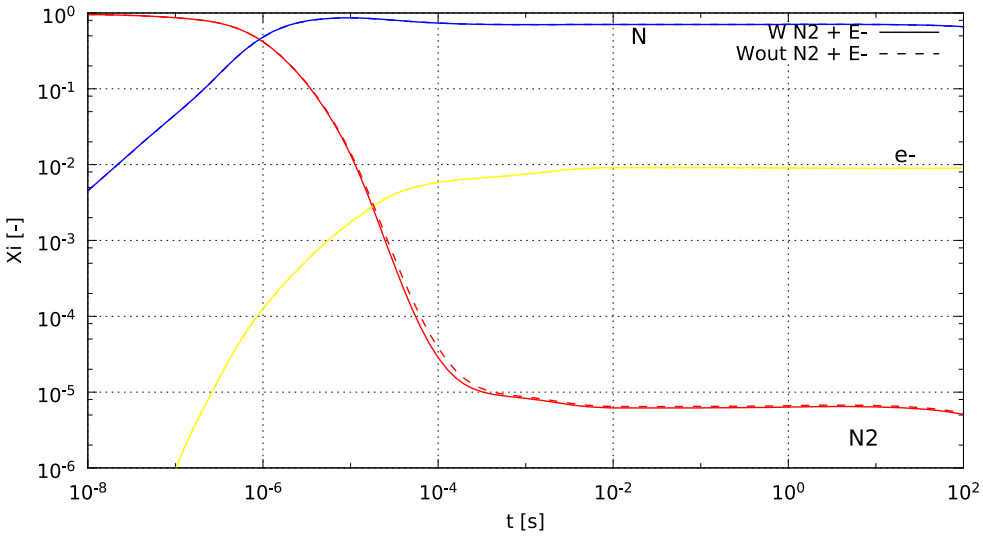

Figure 4: Molar fraction evolution of N_2 with (solid) and without (dashed) dissociation by electronic impact. Upstream conditions of $T = 300$ K, $p = 13$ Pa and 98% of N_2 and 2% of CH_4 in flow mass, shock speed $u = 9$ km/s.

3.2 Harmonic Oscillator model for electronic excited species

In this section we present the analysis and implementation of the Harmonic Oscillator model in SPARK code for ESS simulations. We start by briefly motivating this addition in section 3.2.1 and a small analysis is presented in section 3.2.2. A comparison of the analytical model and the Harmonic Oscillator model is done in section 3.2.3.

3.2.1 Motivation

The Harmonic Oscillator model was introduced in this work in subsection 2.3.1. The usage of this model allows a more efficient computation of the vibrational partition function without *a priori* knowing the vibrational levels of a species. For ESS species, this model was implemented in SPARK code during the course of this work. This is a great advantage for species for which SPARK database is incomplete. However, for higher vibrational levels of a species the Harmonic Oscillator is no longer a good approximation. This can become an important factor for higher internal temperatures of the species leading to error in ESS simulations. The following analysis is then motivated by the desire to characterize this error and understanding the limitations of using the Harmonic Oscillator as a substitute of the analytical computation of the vibrational partition function.

3.2.2 Analysis

In this subsection we analyze the impact on the results from computing the vibrational partition function through the Harmonic Oscillator and from the vibrational levels. Keep in mind that this analysis is restricted to species which have their vibrational levels included in SPARK database, otherwise a comparison would not be possible. In figure 5, the vibrational partition function of N_2(X) is plotted, computed with the Harmonic Oscillator model and with the vibrational levels. The disagreement of the two models is clear at high temperatures ($T > 6 \times 10^4$ K) but acceptable at low temperatures ($T < 4 \times 10^4$ K). In the lower temperature range, the Harmonic Oscillator seems a good approximation. The electronically excited states of N_2 follow the same trend as in figure 5. The impact of this difference in the backward rate, computed from the equilibrium constant and the forward rate can be seen in figure 6. Even for higher temperatures, the difference is not great from one model to the other even at higher temperatures when the divergence is the greatest. This suggests that using the Harmonic Oscillator model in place of the analytical computation we will not introduce large errors, even at higher temperatures. After this brief analysis, we are ready to compare the results in simulation, which is done in the next subsection.

3.2.3 Comparison

In figure 7, the temperature evolution of an 98% N_2 and 2% CH_4 mixture ESS simulation at a shock speed of 9 km/s is presented. The solid curves represent the calculation with the Harmonic Oscillator model only while the dashed curves use the analytical calculation when the vibrational levels are available in SPARK's

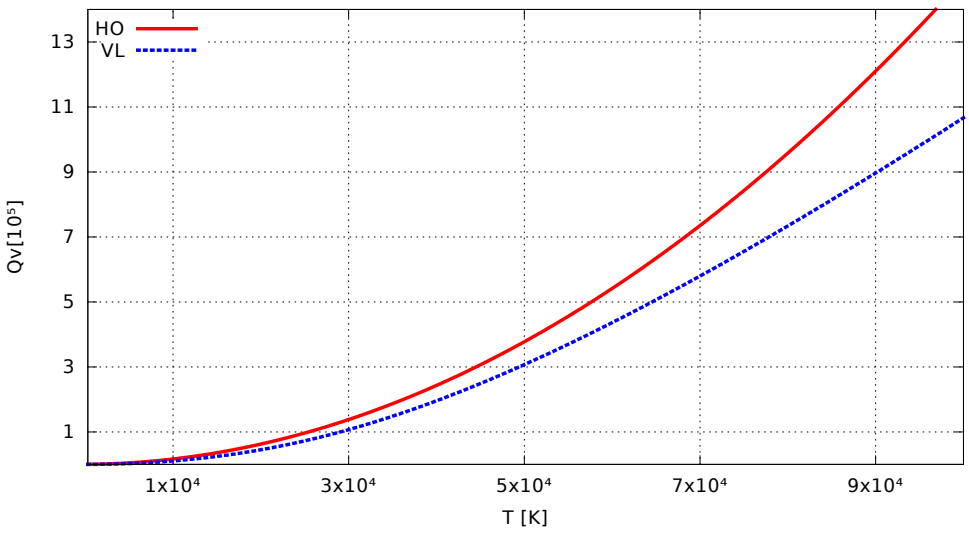

Figure 5: Vibrational partition function of N_2(X) computed through the Harmonic Oscillator (solid line) and the vibrational levels (dashed line).

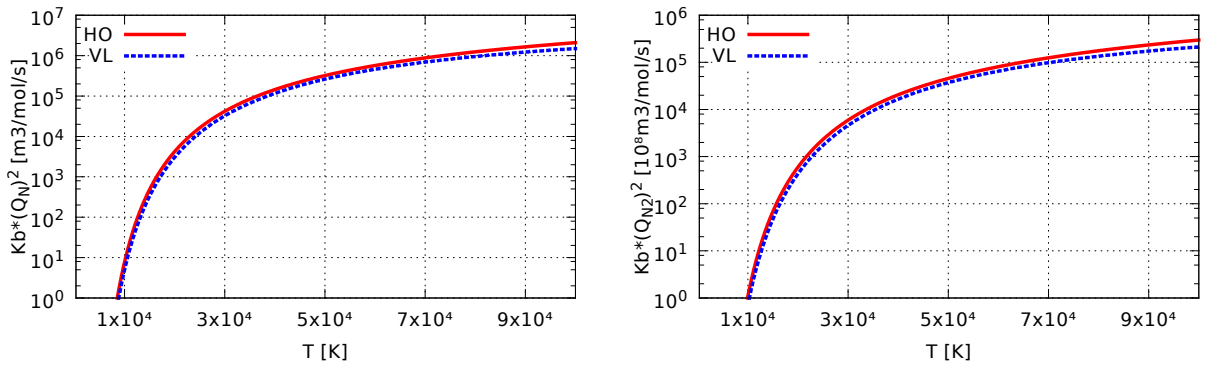

(a) Backward rate for dissociation of N_2(X) by impact of atomic species.

(b) Backward rate for dissociation of N_2(X) by impact of molecular species.

Figure 6: Impact of different models on the computation of backward dissociation rates of different N_2 dissociation mechanisms.

database. It can be seen right away that the differences between the two simulations are not very large. The temperature profile also gives us a clue why: the temperature as a maximum at around 37000 K which looking back at figure 5 reveals that the differences between the model and the analytical calculation are not significant for the present purposes. This is confirmed by the agreement between the two models in figure 8 where the molar fractions of some species are plotted. The greatest difference is in the population of N_2. This makes sense as it is the specie which has the most complete database of vibrational levels in SPARK. We can then say that at least for the purposes of this work the Harmonic Oscillator is a good approximation for the analytical calculations.

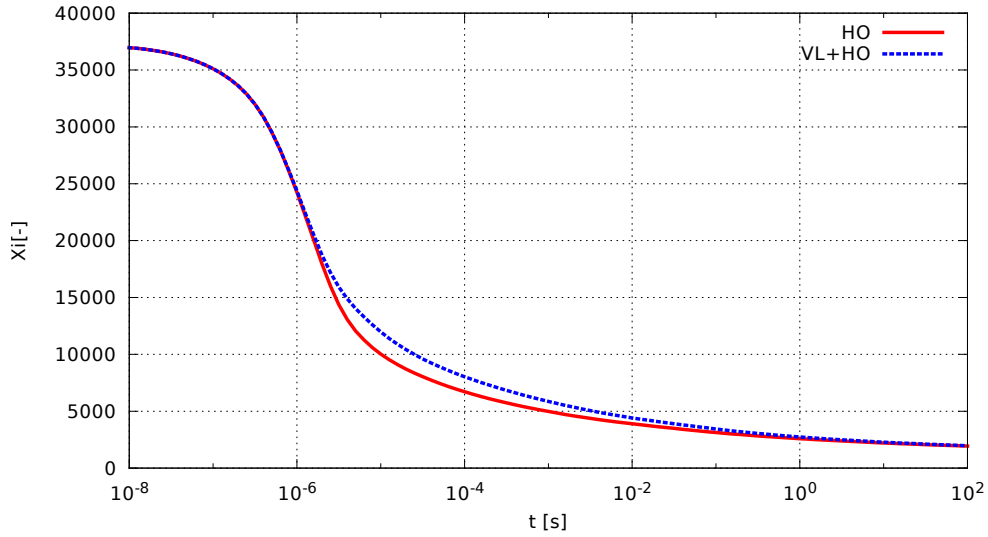

Figure 7: Time evolution of the temperature using partition function computed through the harmonic oscillator (red, solid) and the vibrational levels (blue, dashed)

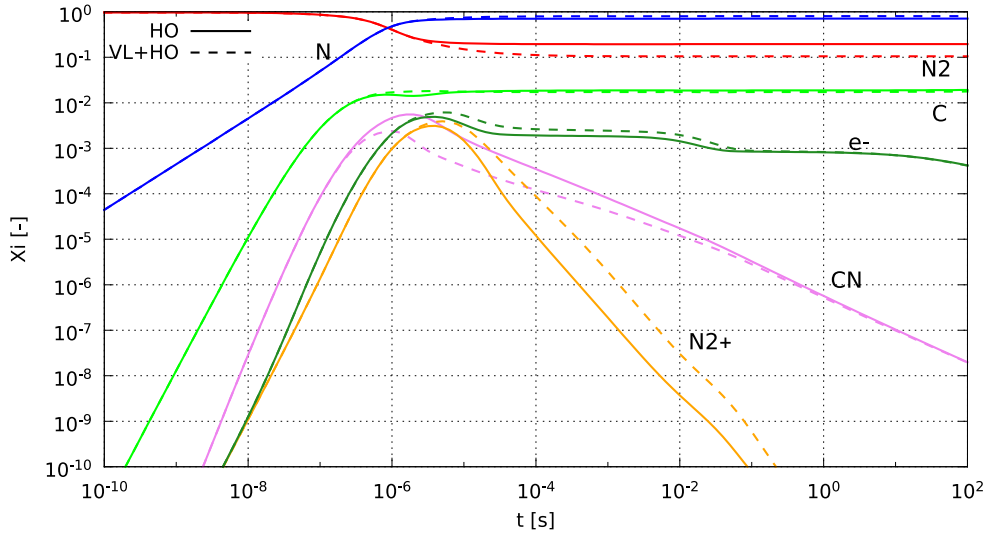

Figure 8: Molar fraction evolution of selected species using partition function computed through the harmonic oscillator (solid) and the vibrational levels (dashed)

3.3 Spontaneous emission processes

This section details the author's contribution to the spontaneous emission modeling in ESS and VSS simulations. We discuss the motivation in section 3.3.1. We describe the method on how spontaneous emission modeling was improved in section 3.3.2. Finally we briefly compare simulations with and without this process in section 3.3.3.

3.3.1 Motivation

Radiative processes are critical in fast entry flows. Depending on the conditions, radiative heating of a thermal protection can become the dominant mechanism of heating. The energy leaking out of the flow can significantly lower the temperature downstream of the shock. It is then in our utmost interest to model correctly radiative processes as accurately as possible.

The Einstein coefficients are probabilities of transitions occurring in excited states to lower energy states of species (known usually within 5-20% accuracy)[2]. Typical models account only for the inclusion of the A_{00} Einstein coefficient for the sake of simplicity, since this is done typically for low temperature applications where the ground vibrational level is the most populated level. Other possible approach would be to determine the lifetime of an excited specie as in [6] and use its inverse as the probability of radiative decay. Both approaches neglect the higher vibrational levels and thus the higher indexed entries in the Einstein coefficient matrices. This can lead to inaccuracies at high temperature when the contribution of higher vibrational levels become more important.

It would be possible to use the whole of the Einstein coefficients matrix to model vibrational state specific radiation. This however either implies that radiative species need now to be modeled as VSS which is computationally expensive or a Boltzmann approximation needs to be assumed for the vibrational levels. Here, we use the latter approach.

3.3.2 Method

The present approach is based on the assumption that at any time radiative species in the flow, the emission probabilities can be modeled as having a Boltzmann distribution over the vibrational levels. The sum of the possible radiative transitions for a given excited state e' is given by:

$$A^*_{e'\to e''}(T) = \sum_{v'} \frac{Q_{e'v'}(T)}{\sum_{v'} Q_{e'v'}(T)} \sum_{v''} A_{e'v'\to e''v''}. \tag{26}$$

$A^*_{e'\to e''}$ is called the equivalent Einstein coefficient for the electronic transition $e' \to e''$ which is dependent on the temperature. The equivalent Einstein coefficients were computed for the transitions N_2(C $\longrightarrow$ B), N_2(B $\longrightarrow$ A), CN(B $\longrightarrow$ X), CN(B $\longrightarrow$ A) and CN(A $\longrightarrow$ X). This calculation uses energy level information that taken from [11, 12, 13] for N_2, from [11, 14, 15] for CN, and Einstein coefficients from [14] for CN and [16] for N_2. The most recent data was used when available.

[2]Private communication with Lino da Silva.

Figures 9 and 10 show the plots of the equivalent Einstein coefficients as a function of temperature. These plots already suggest the relative importance of some transitions against others. Namely, transitions $N_2(C \longrightarrow B)$ and $CN(B \longrightarrow X)$ seem to be more intense than others. The curves in figures 9 and 10 were then fitted to a 9th order polynomial rate. The results of these fits are presented in appendix B.4.

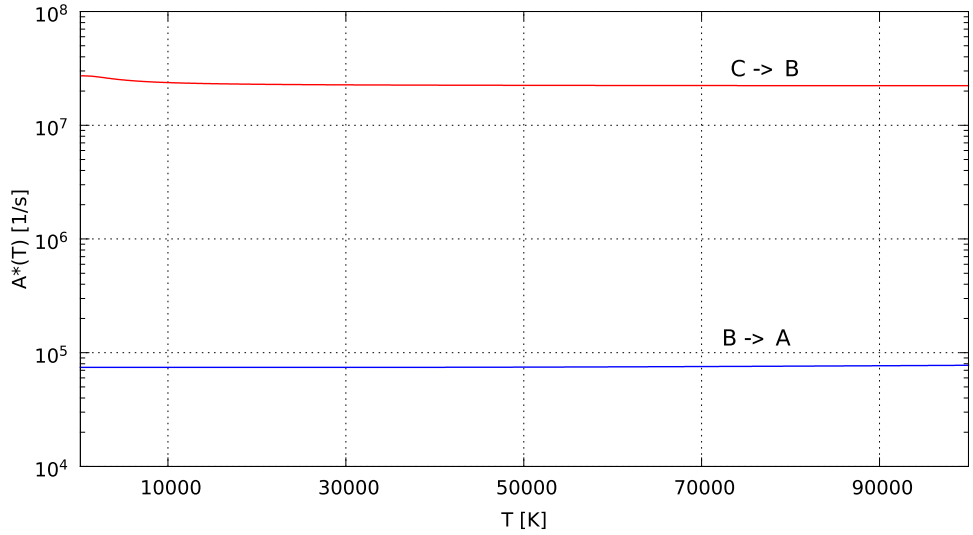

Figure 9: Equivalent Einstein coefficients for $N_2(B \longrightarrow A)$ and $N_2(C \longrightarrow B)$ transitions.

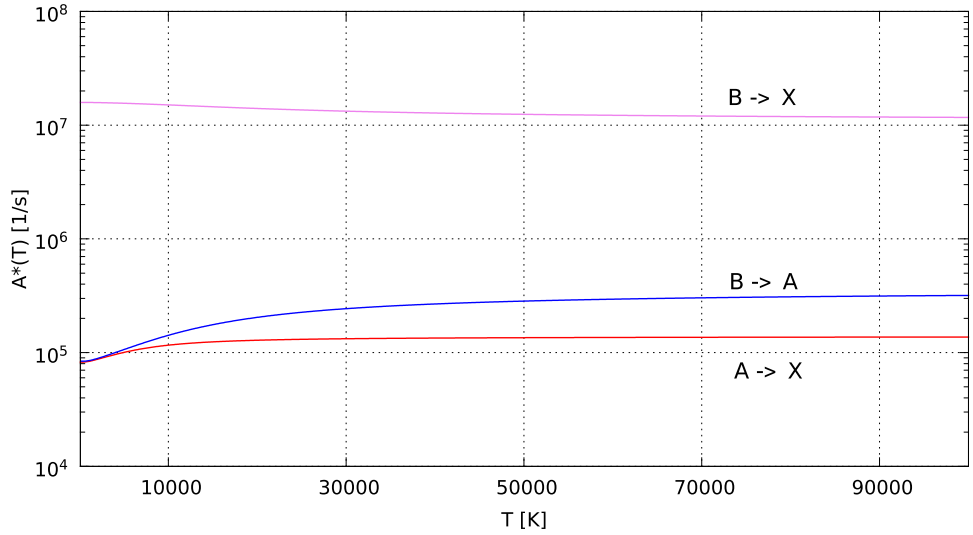

Figure 10: Equivalent Einstein coefficients for $CN(A \longrightarrow X)$, $CN(B \longrightarrow A)$, $CN(B \longrightarrow X)$ transitions.

3.3.3 Comparison

Figure 11 shows the time evolution of temperature of a simulation entry at 5.15 km/s using either the constant rates for the spontaneous emission provided in [6] or the 9th order polynomial coefficients computed in the course of this work. There are some differences between the temperature of the flow when using one model or the other. The constant rates model seems to place greater power in radiative decay, letting the flow to have less available energy for chemical reactions. However, the difference between temperatures is not big enough to produce any significant changes in the molar concentration of species as can be seen in figure 12. In figure 13, the time evolution of the mass fractions of some electronic levels are plotted for a simulation of a shock speed at 5.15 km/s. Due to the different probabilities of spontaneous emission processes occurring for the two different models, the population levels of excited electronic levels will depopulate differently and produce distinctive excited population occupations. The equivalent Einstein coefficient takes into consideration higher vibrational levels with smaller probabilities of decaying to a lower electronic level. This will lead to the differences observed in figure 13.

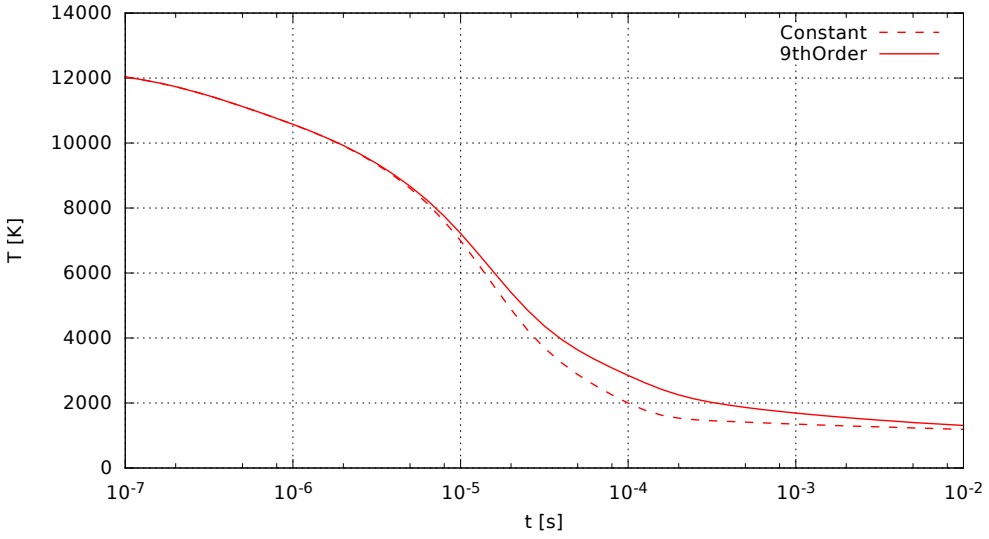

Figure 11: Temperature for simulation of a shock speed at 5.15 km/s with a constant A_{00} Einstein coefficient (dashed), and a 9th order polynomial equivalent Einstein coefficients (solid) for spontaneous emission.

As expected spontaneous emission is a crucial process that bears a heavy influence in the post-shock equilibrium of the flow. We have computed through this method a simplified version of the Einstein coefficient matrices into a *pseudo*-temperature dependent rate. This accounting of the higher vibronic levels of the excited species although not impacting the macroscopic properties of the gas it does change the magnitude of the peak population of electronic excited species.

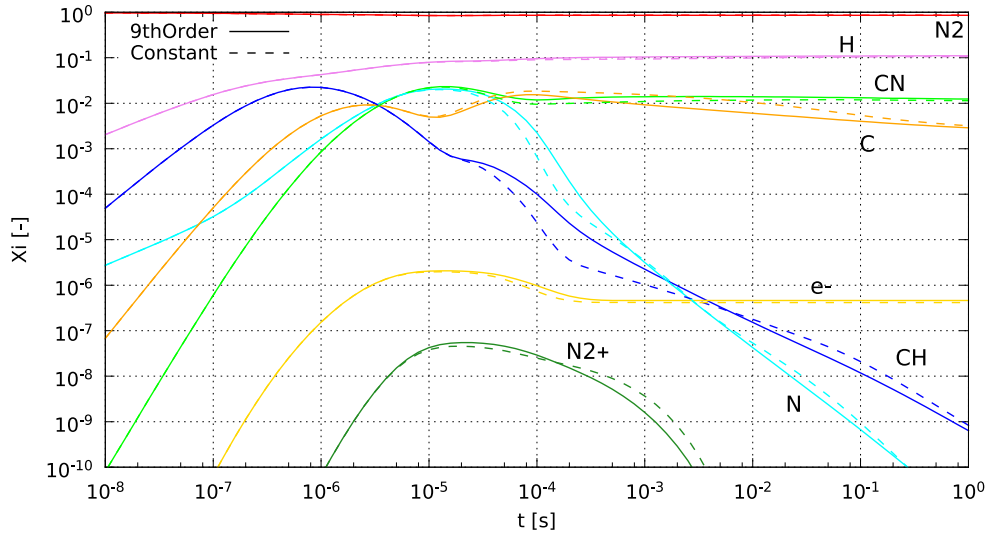

Figure 12: Mole Fractions of selected species for simulation for a shock speed at 5.15 km/s with a constant A_{00} Einstein coefficient (dashed), and a 9th order polynomial equivalent Einstein coefficients (solid) for spontaneous emission.

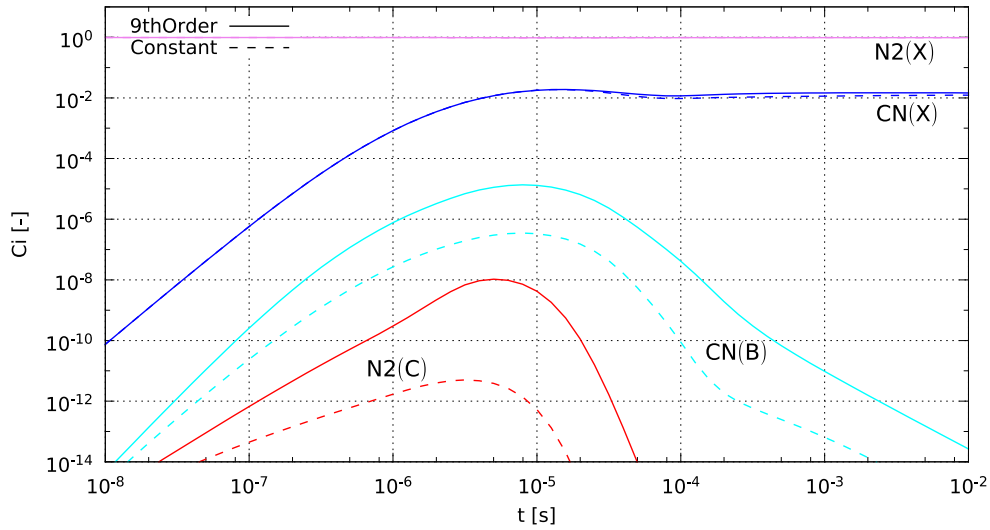

Figure 13: Mass Fractions of internal levels N_2(C), N_2(X), CN(B) and CN(X) for a simulation of a shock speed at 5.15 km/s using the constant Einstein coefficient A_{00} (dashed) and a 9th order polynomial equivalent Einstein coefficients (solid) for spontaneous emission.

3.4 Vibrational redistribution of reaction rates

This section presents the personal contribution of the author to the improvement of vibrational kinetic modeling. The focus is made on the computation of vibrational state specific rates from global or electronic state-specific rates. After explaining the motivations for obtaining such data in section 3.4.1, the vibrational redistribution procedure is described in section 3.4.2. The limitations and known issues of this approach are discussed in section 3.4.3, while the obtained results are presented in section 3.4.4.

3.4.1 Motivations

When dealing with internal modes of chemical species, we need to accordingly update the thermodynamic models as discussed in section 2.3.1. What was not mentioned earlier, is that the conversion to state-specific simulations also requires updates in the applied kinetic models. The focus of this section is the expansion of global or ESS chemical-kinetic rates to vibrational state specific rates, a process which is called vibrational redistribution.

Each global rate is based on the assumption that the internal modes of chemical species are described by a Boltzmann distribution function. Electronic state specific rates are associated to the electronic levels of the species without any *a priori* information on the vibrational mode. Vibrational state specific provides the most accurate description of the kinetic processes in a non-equilibrium gas without any assumption on the distribution of the species internal levels. The downside of this detail is that the determination of actual values for vibrational specific reaction rates is quite difficult. These rates are usually unknown and additional assumptions need to be introduced to determine them. The theoretical basis of this vibrational redistribution and its methodology is explained in the following section.

3.4.2 Redistribution methodology

The procedure used to vibrationally redistribute a reaction rate depends on whether the vibrational state-specific species is a reactant or a product. These two situations are referred as the *reactant case* and the *product case*. For each of these two cases, the actual expression of the vibrationally-resolved rate is deduced by a physical analysis of the energy diagram associated with the considered process. It is found that the rate expression depends on the reaction's activation energy, which depends on the vibrational state of the molecule.

Reactant case: This case refers to kinetic processes in which the vibrational state-specific species is on the reactant side of the reaction. As an example, we take an electronic excitation process for which the rate is only known for the electronic states e' to e'':

$$\mathrm{X_2}(e') + \mathrm{M} \rightleftarrows \mathrm{X_2}(e'') + \mathrm{M}. \tag{27}$$

X_2 is an arbitrary molecular specie and e', e'' two different excited states. M is a generic collisional partner which can be either an electron or a heavy specie. This reaction is unsuited if we want to model $X_2(e')$ as a vibrational state specific species. We want to model a set of reactions that accounts for vibrational excitation such as:

$$X_2(e', v) + M \rightleftarrows X_2(e'') + M, \tag{28}$$

until we reach the dissociation vibrational level of specie $X_2(e')$, v_{max}. Reaction (27) is described by an Arrhenius rate repeated here for convenience,

$$k = AT^n \exp(-\theta/kT),$$

where A, n and θ are coefficients determined experimentally or by theoretical models. The vibrational redistribution procedure is based on the physical meaning of θ, which corresponds to the activation energy of the reaction. This quantity is defined as the energy difference between the reactants and the products. If sufficient energy is provided to the system $X_2(e', v) + M$, the transition takes place leading to the formation of the products. here, the energy gap E_g, is the amount of energy between the products and the reactants for each vibrational state.

Figure 14 illustrates the energy difference of the reactants on the left and the products on the right. The ESS rate provided for reaction (27) is strictly valid for the first vibrational level $v = 0$. The energy gap E_g is equal to θ. For the second vibrational level, the energy gap between reactants and products is now smaller by the amount $\varepsilon_{v=1}$, ε_v being the vibrational energy associated to vibrational level v from the ground state. The new energy gap is then $E_g(v) = \theta - \varepsilon_v$. While the energy gap is positive, the reaction is endothermic and the rate is written

$$k = AT^n \exp(-E_g(v)/kT), \tag{29}$$

until the reaction becomes exothermic at level v_+. This implies that the energy gap is zero as the system is already in the highest energy it can reach. The rate is then written

$$k = AT^n, \tag{30}$$

for an exothermic reaction.

Product case: This case refers to chemical-kinetic processes in which the vibrational state-specific species is on the product side of the reaction. To illustrate this, we take as example an electronic de-excitation process,

$$X_2(e'') + M \rightleftarrows X_2(e') + M. \tag{31}$$

In this case, we want to have a list of reactions of the type

$$X_2(e'') + M \rightleftarrows X_2(e', v) + M, \tag{32}$$

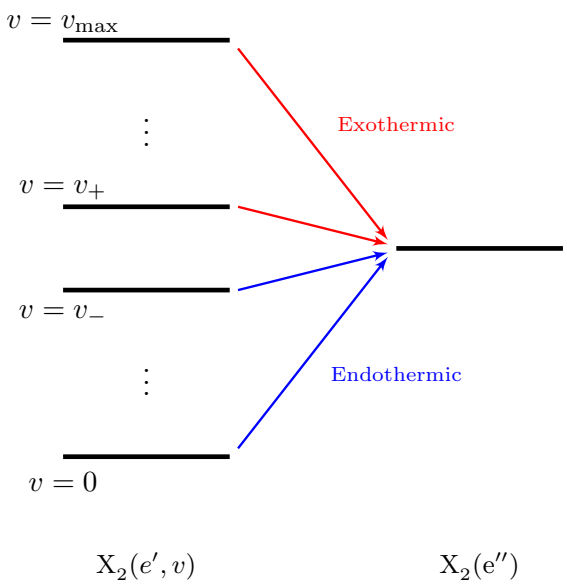

Figure 14: Energy transition diagrams for the two reactions showing the vibrational structure of the electronic states of the reactant species.

until the maximum vibrational level, v_{max} is reached. The same concepts of the previous case apply here. The reaction is described by an Arrhenius law and because it is an exothermic reaction, the energy gap is zero. The Arrhenius rate hence is

$$k = AT^n. \tag{33}$$

Figure 15 represents the energy diagram of the system in this case. As before, the rate of reaction (31) only applies to the first vibrational level. In this case however, for the first vibrational level the energy gap doesn't decrease rather, since it stays zero. What does decrease is the energy released by the reaction. In this situation the rate stays the same as equation (33) until it stops being exothermic in vibrational level v_+. For this level, reaction (31) becomes endothermic and the energy gap stops being zero. For levels v_+ to v_{max}, the rate is given by

$$k = AT^n \exp\left(-E_g(v)/kT\right), \tag{34}$$

where the gap energy is now $E_g = \varepsilon_v - E_0$, E_0 being the energy difference between the reactants and the products for the first vibrational level.

3.4.3 Limitations and known issues

The procedure described above is straight forward to apply since only one coefficient of the modified Arrhenius law need to be modified. However, although the derivation of the vibrational redistribution method has been based on physical arguments, the approach still suffers from a physical inconsistency.

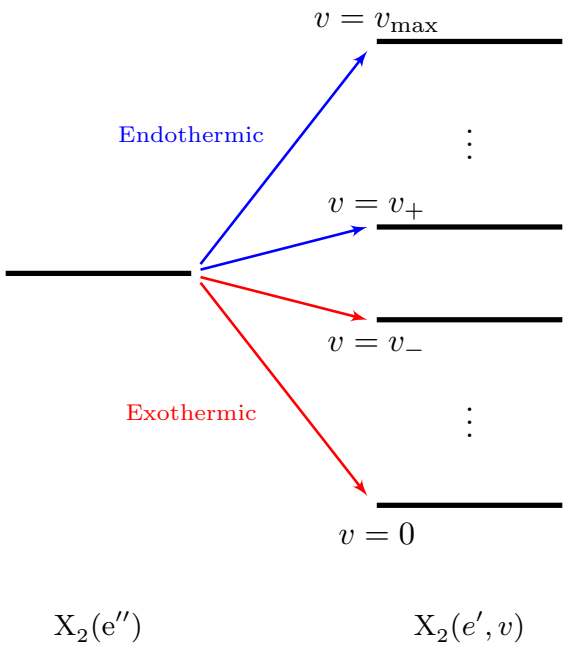

Figure 15: Energy transition diagrams for the two reactions showing the vibrational structure of the electronic states of the product species.

In order to explain the deficiency of the proposed method, let us consider an arbitrary diatomic species excited to the electronic level e', $\mathrm{X}_2(e')$ and $X_2(e', v)$ the vibrational level v of the e' electronic level. The vibrational redistribution procedure developed in the frame of this work enables to compute – or at least, to approximate – a set of vibrational state-specific rates $k_{X_2(e',v)}$ from a known electronic state-specific rate $k_{X_2(e')}$. The reverse operation, that is computing an electronic state-specific rate from a set of vibrational state-specific rates, is represented by the following relation:

$$k_{X_2(e')} = \sum_v k_{X_2(e',v)} \cdot \frac{[\mathrm{X}_2(e', v)]}{[\mathrm{X}_2(e')]} \tag{35}$$

where the brackets $[\cdot]$ represent molar concentrations. Assuming a Boltzmann distribution of the vibrational levels of $X_2(e')$, the concentrations ratio in (35) can be substituted by the Boltzmann equilibrium relation, leading to:

$$k_{\mathrm{X}_2(e')} = \sum_v k_{\mathrm{X}_2(e',v)} \frac{\exp\left(-\frac{\varepsilon_v}{kT}\right)}{Q^{\mathrm{vib}}_{\mathrm{X}_2(e')}} \tag{36}$$

where $Q^{\mathrm{vib}}_{\mathrm{X}_2(e')}$ is the vibrational partition function of $\mathrm{X}_2(e')$. What this expression tells us is that, if the vibrational levels actually follow a Boltzmann distribution, then a VSS simulation using a set of $k_{\mathrm{X}_2(e',v)}$ vibrational state-specific rates should give exactly the same results than a ESS simulation using a single $k_{\mathrm{X}_2(e')}$ electronic state-specific rate. However, equation (36) will not be satisfied using the VSS rates obtained from the current vibrational redistribution method. The consequence of this inconsistency between the electronic

and vibrational state-specific description is that, even in the case of a Boltzmann distribution of vibrational levels (either physically obtained or numerically enforced), the VSS rates will not predict the same results than an ESS simulation. A method which removes this inconsistency can be found in [26] which was not implemented, but should be considered the next step of this work.

3.4.4 Results

It is challenging to evaluate the performance of this model without comparing it to another model built with the same objective. We can either apply rate redistribution models or not. When we don't use vibrational redistribution in the kinetics model, the only VSS rates are those from FHO and Magin's two resonant rates[3]. This is fairly alike to saying that only the first vibrational levels are important in kinetic and chemical processes, besides dissociation and vibrational excitation. We have applied the vibrational redistribution model to $N_2(X)$ as this is the only VSS species in the flow. This approximation ensures the influence of vibrational excited states of $N_2(X)$ on the chemical and kinetic processes, being $N_2(X)$ either a product or a reactant.

Figure 16 represents the time evolution of mole fractions in the gas of selected species for a shock wave speed of 9 km/s. The dashed curves present the results for the kinetic model without vibrational redistribution, while the solid curves include vibrational redistribution. The differences between the two sets are small and suggest that vibrational redistribution does not play an important role in the overall population numbers of the species. This may be either from the insufficiency of the model in portraying the exchange, radical and ionization reactions, or due to the poor contribution that the excited states of $N_2(X)$ have on these reactions in reality. Figure 17 plots the internal and total population numbers of the main radiative species, for the same conditions as in figure 16. Here, the influence of vibrational redistribution is much clear in the magnitude and instant of the peak population of the two internal level populations. This trend is the observed for other internal levels simulated in the same conditions[4] and for simulations with smaller shock speeds. This indicates a coupling between vibrational excitation and electronic excitation, as excited electronic states are associated with the presence of $N_2(X)$ as featured in Magin's kinetic (see appendix B.3). Indeed, from $t = 10^{-8}$ to $t = 10^{-6}$, the first vibrational level of N_2 loses it's prominence and the excited vibrational states become more significant in the flow. This can be seen in figure 18 where the time dependent mass fractions for the first 20 vibrational levels of $N_2(X)$ are plotted. There are not large differences between the population levels obtained using a simulation with and without vibrational redistribution because the vibrational levels of $N_2(X)$ constitute a much higher mass fraction for the gas than the higher electronic levels CN(B) and $N_2(C)$. The vibrational excited states of $N_2(X)$ are then contributing to a more efficient electronic excitation, according to the model of vibrational redistribution.

[3]FHO: A model for VSS rates, in this work applied to $N_2(X)$ dissociation and vibrational excitation. See appendix B.5 for more details. Magin's resonant rates: see appendix B.3

[4]These are not plotted here due to the large number of curves.

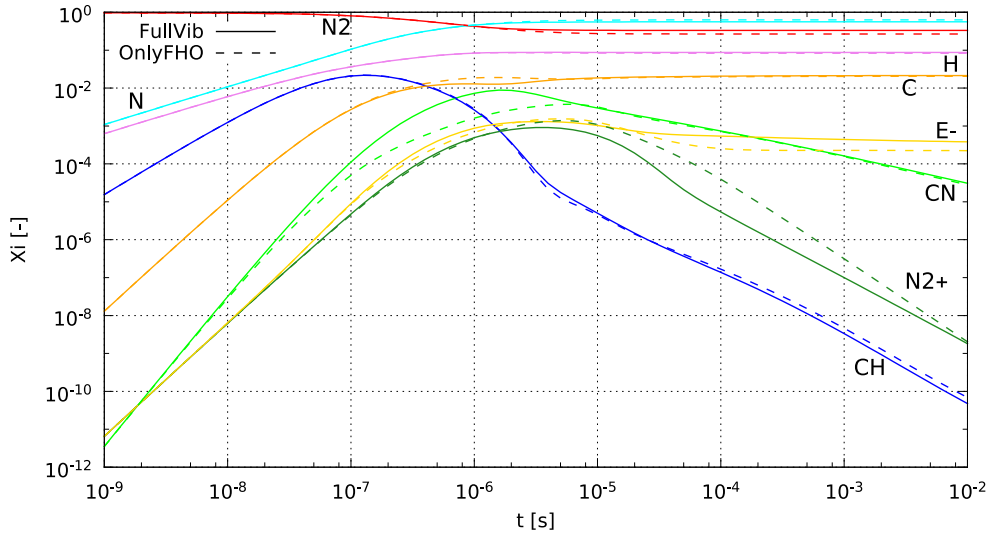

Figure 16: Species mole fractions using the FHO model (dashed) and the FHO model with vibrational redistribution (solid). Upstream conditions: $T = 300$ K, $p = 13$ Pa, $u = 9$ km/s and mass composition 98% of N_2 and 2% of CH_4.

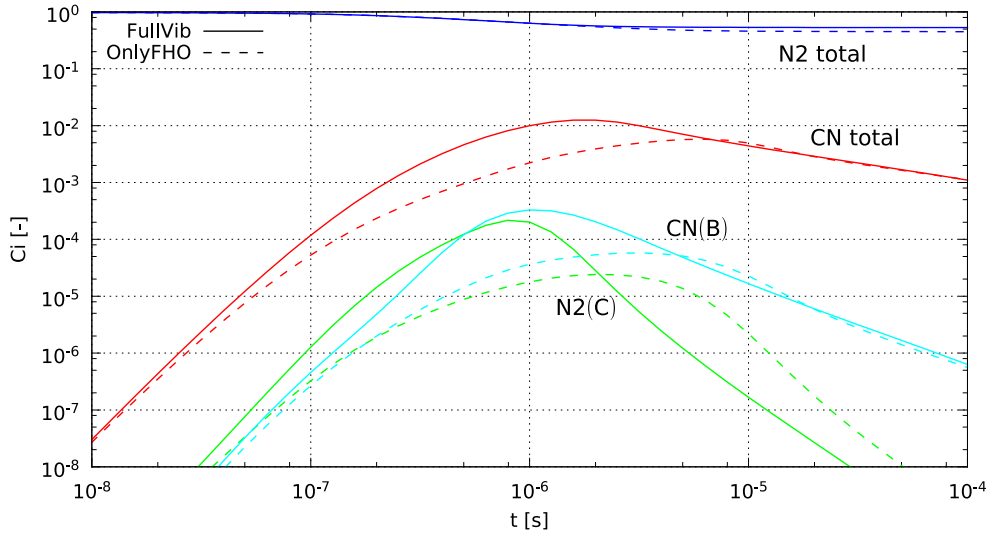

Figure 17: Mass fractions of internal levels $N_2(C)$, CN(B) and general population of N_2 and CN using the FHO model (dashed) and the FHO model with vibrational redistribution (solid). Upstream conditions: $T = 300$ K, $p = 13$ Pa, $u = 9$ km/s and mass composition 98% of N_2 and 2% of CH_4.

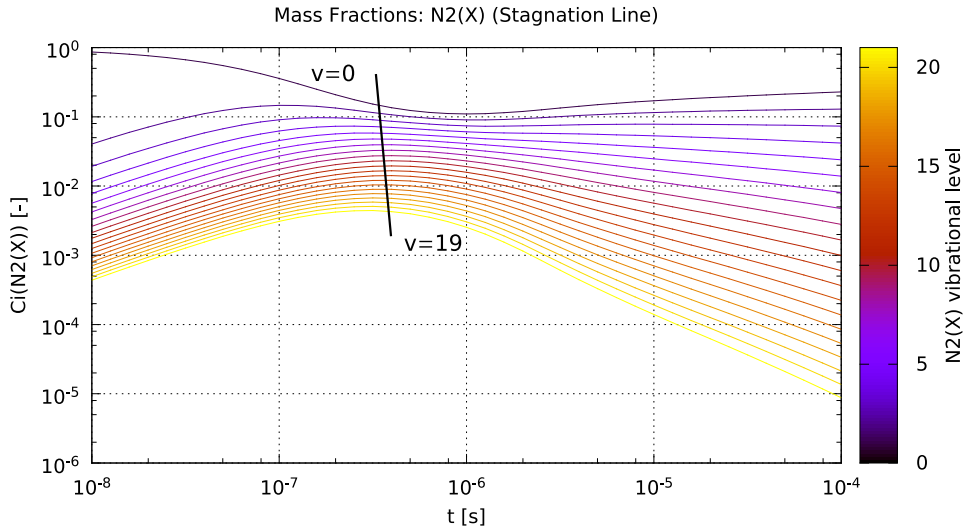

Figure 18: First twenty vibrational states of N_2(X) in a VSS simulation using the FHO model with vibrational redistribution. Upstream conditions: $T = 300$ K, $p = 13$ Pa, $u = 9$ km/s and mass composition 98% of N_2 and 2% of CH_4.

4 Shock tube simulations

4.1 The test matrix

This section focuses on the results obtained from simulations after applying the model improvements discussed in chapter 3. In order to produce meaningful comparisons, all simulations have the following upstream conditions: $T = 300$ K, $p = 13$ Pa, mass composition 98% of N_2 and 2% of CH_4 whereas for the shock speeds we will focus on two cases: 5.15 and 9 km/s. These conditions have been reproduced in shock tubes experiments by Brandis [7].

We will briefly discuss the macroscopic results in section 4.2 (temperature and mole fractions) and then move on to the internal levels of some important radiative species in section 4.3. This is in preparation for the radiation results which will be more focused in section 4.4. These results are more pertinent scientifically, as the ones that can be compared to shock tube experiments.

These simulations will be performed employing two different kinetic models: the Gökçen model, developed for Titan entry applications [5] and Lino da Silva model which updates the Gökçen model for higher temperatures [9], as well as in what concerns the kinetic detail, Boltzmann, ESS and VSS simulations. The details about each kinetic model are presented in appendix B.

4.2 Global results

In figure 19 the macroscopic temperature of the gas is plotted for the shock speeds 5.15 and 9 km/s. Each plot displays Lino da Silva's in solid lines and Gökçen's kinetics in dashed lines. In these two figures there are some trends to be noticed. First, post-shock cooling is generally slower for the Boltzmann model, followed by the ESS and then VSS models. This is in agreement with state-specific kinetics, as endothermic electronic and vibrational reactions favor energy exchanges in the flow, contributing thus to the absorption of translational energy.

A feature of the 9 km/s shock, is that endothermic processes in Gökçen's kinetics lead to a faster temperature decrease than in Lino da Silva's. In contrast, for a shock of 5.15 km/s, both kinetics agree reasonably on the temperature's values. This outlines the feature of Lino da Silva's update to Gökçen kinetics, enforcing the same low temperature behavior but keeping rates physically consistent at higher temperatures. We should therefore expect similar results for low speed shocks at 5.15 km/s but larger discrepancies at 9 km/s.

The dominant difference from the two in shock speeds is the dissociation incubation time. As will be corroborated in later figures, dissociation is one of the main endothermic processes. It is clear that for lower shock speeds the temperature starts decreasing later than for higher speeds. This implies that greater availability of energy fosters dissociation and other endothermic processes, thus decreasing the temperature. The dissociation incubation time is then greater for smaller energies.

In figure 20 we plot the mole fractions of selected species for the two shock speeds and different kinetic models. The dissociation of N_2 is not noticeable for a 5.15 km/s shock as we can conclude observing the

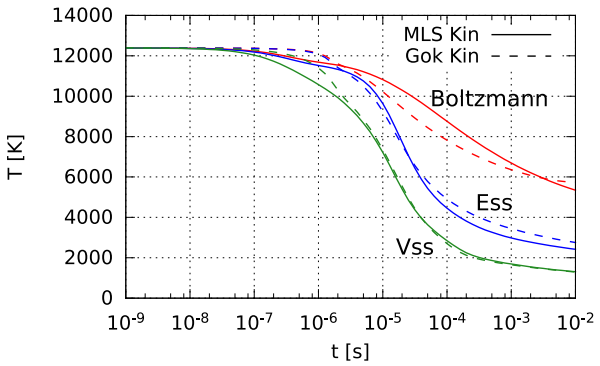

(a) Shock speed of 5150 m/s.

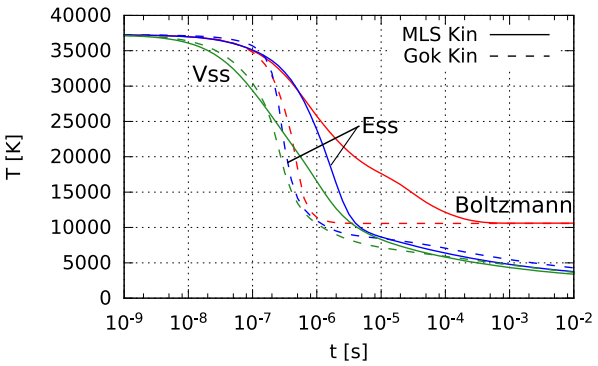

(b) Shock speed of 9000 m/s.

Figure 19: Temperature temporal evolution using Lino da Silva's (solid) and Gökçen's (dashed) kinetics, considering Boltzmann, ESS and VSS models and two shock speeds.

creation rate of N atoms in the figures. The peaks of the N atoms populations are compatible with the temperature decrease in figure 19. Also visible, is the decrease of ionization degree (10^{-4}, 10^{-5}, 10^{-6}) as the kinetic model goes from Boltzmann to VSS. The VSS simulation has a fairly low degree of electrons for 5.15 km/s whilst the Boltzmann has a population of electrons two orders of magnitude above. This can be explained by the available energy in the flow. Once dissociation is fully established, ionization sets in and so more energy is available more ionization exists.

In contrast with the 5.15 km/s simulation, the 9 km/s has a much larger electron population. The dissociation of N_2 is also much more pronounced than at lower shock speeds, with N becoming the major species produced around $t = 10^{-6}$. The idea that the Boltzmann simulation has reached equilibrium conditions is reinforced by the molar fractions that also eventually become constant. This equilibrium is much more pronounced in Gökçen's kinetic scheme probably due to the non-physical rates used in this model which force the gas to reach equilibrium conditions much faster. Another clue to the unphysical rates of Gökçen's kinetics is the recombination of electrons and ions. For lower speeds in figure 20, the electron population is stable at the later temporal stages of the gas. At higher speeds however, Gökçen's electron populations are decreasing while Lino da Silva's are constant. This would only make sense if the energy available was significantly lower from one kinetic model to the other. This is not verified and adds to the case of unsuitability of Gökçen's kinetics for higher temperatures.

We may now draw a more general conclusion on Gökçen's and Lino da Silva's kinetics as well the kinetic levels of detail, Boltzmann, ESS and VSS. Gökçen's kinetics appear to be inadequate for higher temperatures. This was seen regarding the disagreement of population levels of electrons and the difference in the temporal evolution of temperature for higher shock speeds. VSS simulations, include a large number of V-T endothermic processes that the ESS and Boltzmann models are lacking, favoring faster decrease of the plasma temperature downstream of the shock.

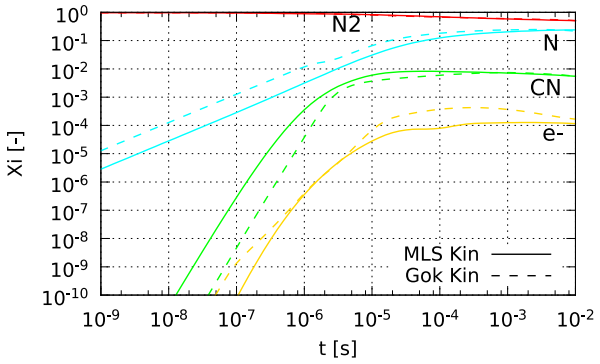

(a) Boltzmann simulation at 5.15 km/s.

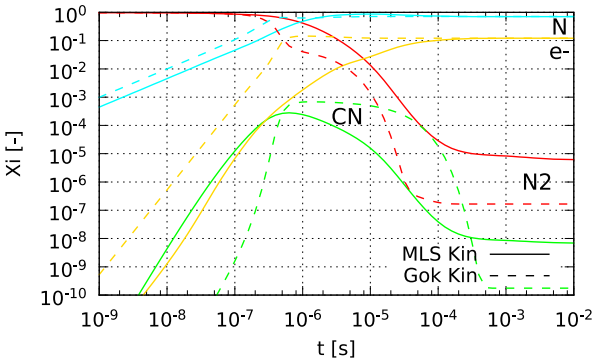

(b) Boltzmann simulation at 9 km/s.

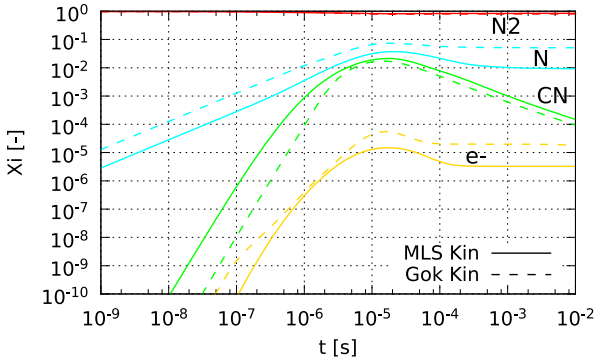

(c) ESS simulation at 5.15 km/s.

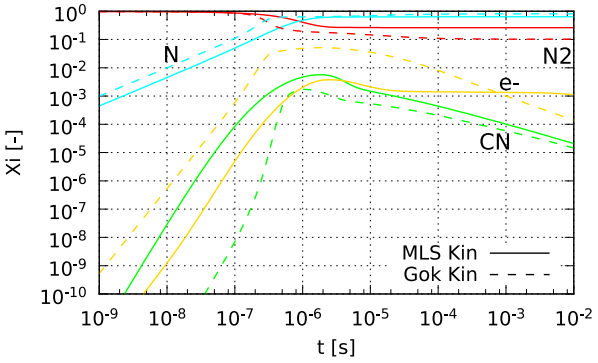

(d) ESS simulation at 9 km/s.

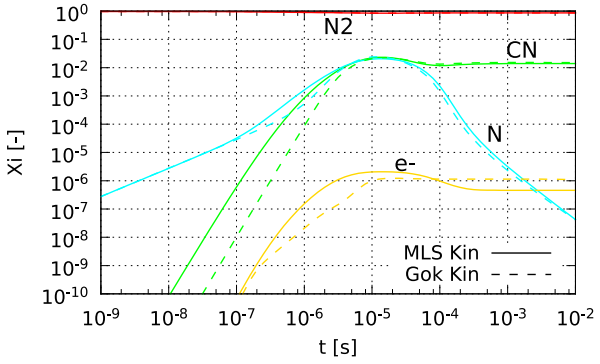

(e) VSS simulation at 5.15 km/s.

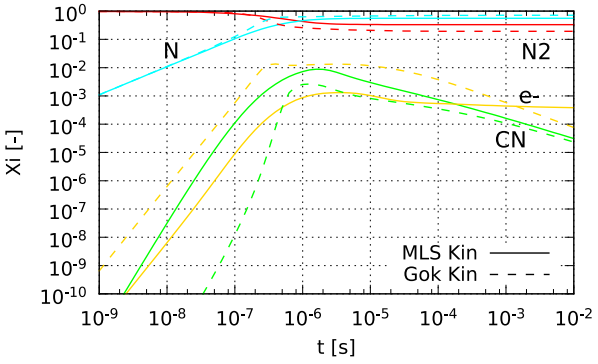

(f) VSS simulation at 9 km/s.

Figure 20: Time evolution of the mole fractions of selected species using different kinetic models for two shock speeds.

4.3 Excited species populations

In the previous subsection we have analyzed a case showing the unsuitability of Gökçen's kinetics at high temperatures, being the subsection more concerned with the macroscopic properties of the gas. In this subsection we will be analyzing the populations of the species excited states which are key to the radiative characteristics of the gas.

Radiative processes are intimately linked with these excited electronic states. In figure 21 the mass fraction of stronger emitting species and their ground levels are shown. There is a good agreement across kinetic details ESS, VSS either for Gökçen and Lino da Silva models, for a shock speed of 5.15 km/s. At this temperature $N_2(X)$ makes up for most of the mass and is barely visible in the top of the graphs. From this, we are expecting a proximity on the respective radiative curves for a 5.15 km/s shock. On the contrary, a 9 km/s shock, there is no agreement between the different models and kinetics. The order of magnitude of the peak populations is the same but there is a discrepancy in the time scale across the models. This will have a direct impact on the radiative properties of the gas.

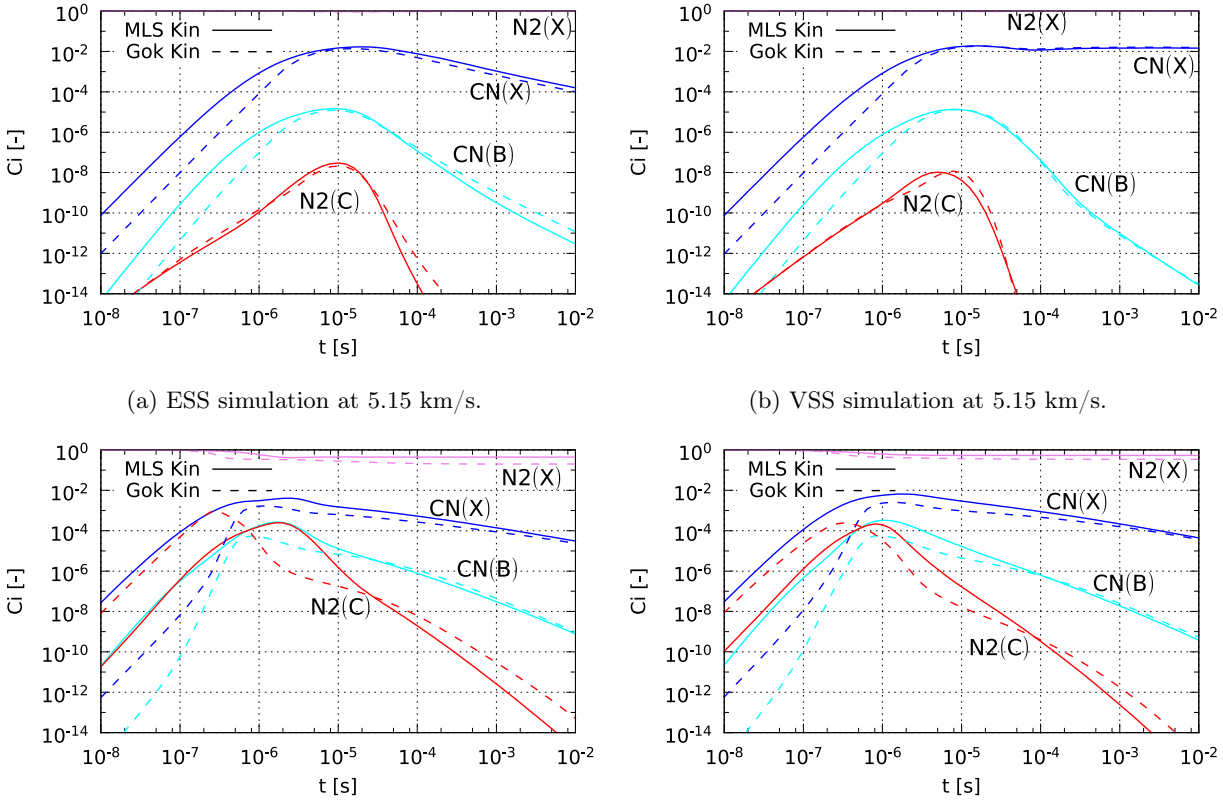

(a) ESS simulation at 5.15 km/s.

(b) VSS simulation at 5.15 km/s.

(c) ESS simulation at 9 km/s.

(d) VSS simulation at 9 km/s.

Figure 21: Time evolution of the mass fractions of selected electronic levels of N_2 and CN for ESS and VSS simulations using Gökçen and Lino da Silva models.

In figures 22, the mass fraction of the vibrational levels of $N_2(X)$ is shown. Both shocks at 5.15 km/s

have very similar behaviors. This is not surprising as the vibrational excitation is mostly dictated by the FHO model, which both simulations share. Both populations distributions are vibrationally excited in the same way and dissociation starts at the same time in accordance with figures 20 and 19. By the end of the simulation, the population levels of higher vibrational levels seem to be depopulated while those from lower levels remain stable. The resonant reaction involving CN(X) and the 5th vibrational level of N_2(X) has a slight influence on the population of vibrational level $v = 4$ at the end of the simulation for 5.15 km /s shocks but there is no population inversion. The resonant reaction of $v = 11$ and CN(X) has no visible influence.

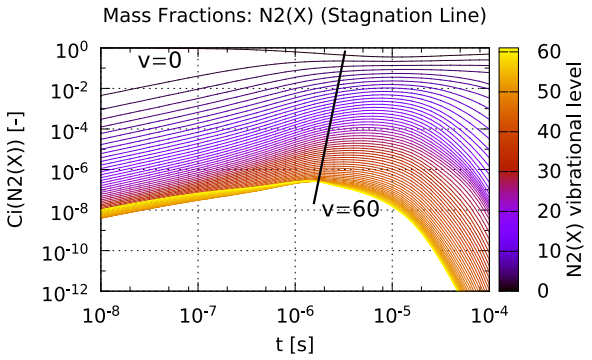

(a) Distribution, Gökçen kinetics at 5.15 km/s.

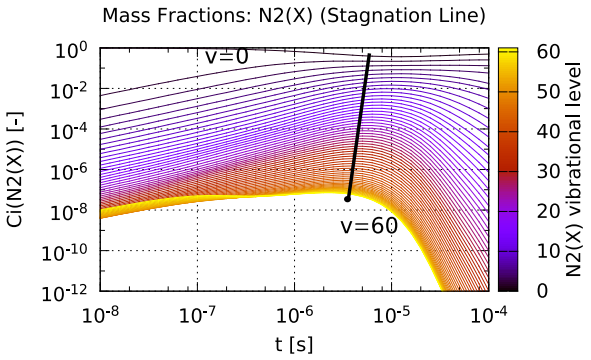

(b) Distribution, Lino da Silva kinetics at 5.15 km/s.

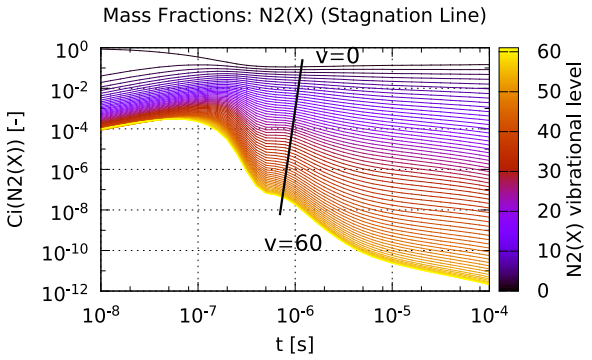

(c) Distribution, Gökçen kinetics at 9 km/s.

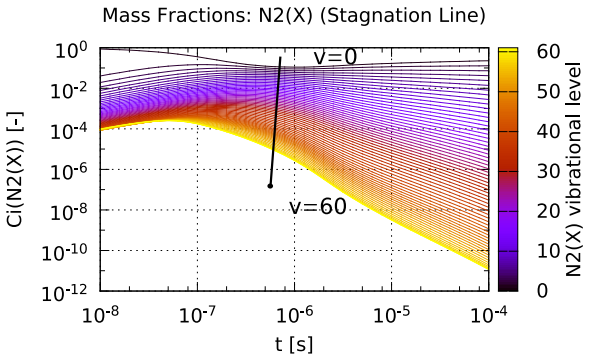

(d) Distribution, Lino da Silva kinetics at 9 km/s.

Figure 22: Distribution of vibrational levels of N_2 for VSS simulations in the case of Gökçen and Lino da Silva models and 5.15 and 9 km/s shock speeds.

For a 9 km/s shock, there is no longer any agreement between the two kinetic models. While the vibrational excitation is the same (due to the shared FHO model), the higher temperatures reached at this shock speed yield very different N_2 dissociation regimes. A bump in the vibrational distribution for the Gökçen kinetic can be observed around $t = [10^{-7}, 10^{-6}]$. At this time the explanation for this sort of plateau is unclear. We can only speculate that this feature is due to a different interaction of the vibrational redistribution model with the original chemical-kinetic model of Gökçen in comparison to Lino da Silva. In contrast, Lino da Silva kinetics exhibits a smooth temporal evolution.

4.4 Post-shock radiation

In figure 23, the post-shock radiative intensity is plotted for every thermodynamic and kinetic model for the two shock speeds. The calculated results are compared with experimental data taken from A. Brandis PhD thesis [7]. Note that our simulations are carried out in a 0D framework. Experimental data is not in the same format as a 0D simulation. In fact, experimental data was presented on a distance scale, by considering the distance from the shockwave. The conversion from distance to a time scale is done assuming a constant shock speed. Also, since the spectral window for the shock tube experiments only covers the spectral range $[310, 450]$ nm, where the only radiation systems are the $N_2(C) \longrightarrow N_2(B)$ (2nd positive) and the $CN(B) \longrightarrow CN(X)$ (violet) systems. This is taken into account in the calculation through a new variable S_{ij} which is 1 if the transition is within the spectral window and 0 if the transition is outside it. S_{ij} is introduced in equation (22).

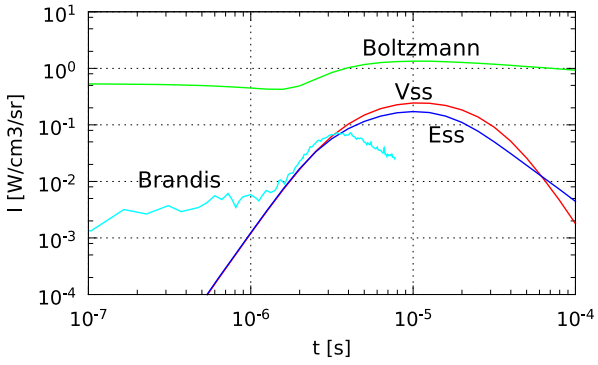

(a) Radiation intensity, Gökçen kinetics at 5.15 km/s.

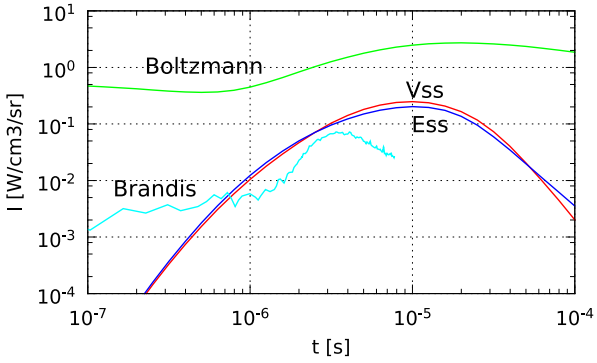

(b) Radiation intensity, Lino da Silva kinetics at 5.15 km/s.

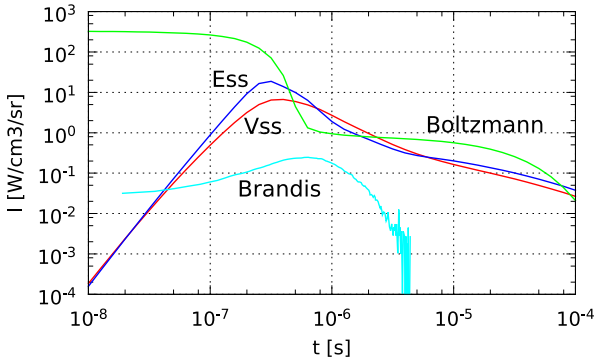

(c) Radiation intensity, Gökçen kinetics at 9 km/s.

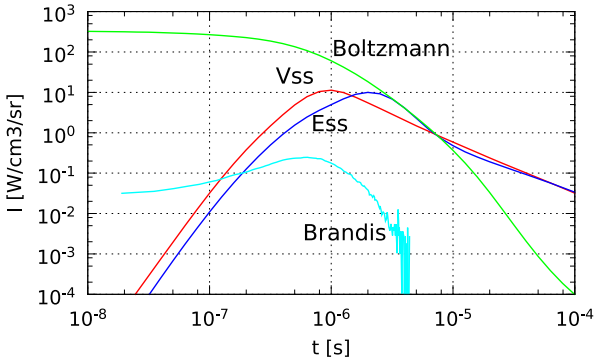

(d) Radiation intensity, Lino da Silva kinetics at 9 km/s.

Figure 23: Total radiation intensity in $[310, 450]$ nm range for several simulations.

The first noticeable difference is that Boltzmann kinetics overpredicts the intensity of radiation. This is expectable since the plasma temperatures is higher for a Boltzmann simulation (see figure 19). Two regimes can also be identified with a change between them at around radiation peak. This is due to the estimation

of electronic levels population. The first regime is dominated by the transition $N_2(C) \longrightarrow N_2(B)$ while N_2 is still the majority population. After the radiation peak, CN is mostly created beginning the second regime associated with the dominating $CN(B) \longrightarrow CN(X)$ transition. At 5.15 km/s, not much N_2 is dissociated, so that the second regime is the sum of both radiative transitions, while at 9 km/s, N_2 and CN sufficiently dissociate such that radiation drops with time. This is in agreement with figure 20 with Boltzmann plots.

The differences between the ESS and VSS results are not important for 5.15 km/s. Both models are in reasonable agreement with the experimental results at this lowest shock speed. This suggests that for lower speeds, there is no advantage in considering vibrational state specific kinetics as a simpler model yields very similar results. As with other results in this chapter, Gökçen and Lino da Silva kinetics agree at lower temperatures. We restate, that 5.15 km/s was the entry point of the Huygens capsule which successfully entered in Titan's atmosphere in 2004.

For a 9 km/s shock, ESS and VSS models for each kinetic scheme seem to have different radiative peak heating. The magnitude between simulated results is precise, but not accurate when taking into account the experimental results. The ESS Gökçen predicts a radiative peak sooner while the ESS Lino da Silva simulation predicts it later when compared with the experiment. The VSS model seems to predict a good radiative peak temporally-wise so, that it is a benefit to use it for higher energies. The time of the peak has been better predicted by Lino da Silva, but this result is not yet very satisfactory taking into account the radiative magnitudes in more detail.

This divergence seems even to be more serious when observing the spectral data from Brandis [7]. As one of the failures of these models, $N_2(C)$ is actually not an observed transition in this spectral data. In this model however, it plays an important contribution. This may be due to the lack of a reaction in our model for the dissociation of $N_2(C)$. Adding this reaction may well hamper the population of this level. Looking back to figures 21 and 22, the $N_2(C)$ mass fraction presents a relative population similar to the higher vibrational levels of $N_2(X)$. If it dissociates as easy as one of the higher vibrational levels, the radiation from the $N_2(C) \longrightarrow N_2(B)$ transition may then become negligible. CN(B) doesn't dissociate as well, but globally the dissociation of this specie is not as dramatic as the dissociation of N_2. The dissociation of CN is also not occurring before radiation peak but after.

Another factor that could further increase the accuracy of this model is an improvement on the vibrational redistribution model employed. The physical lack of physical consistency of this model has been discussed previously. The model could be improved as in [26] to be physically consistent and this might attenuate the magnitude of the radiation peak. Another factor that could be investigated would be higher shock speed simulations and cross-checking with other experimental data using other initial gas compositions. This could potentially lead to improved model corrections and/or to a global validation of it.

5 Conclusions

The two main objectives of this work have been partially achieved. To summarize the contributions made to the following:

- The forward rate of reaction $N_2 + e^- \rightleftarrows 2\,N + e^-$ was computed and verified not to have a significant impact in the mole concentrations of the different species. It is included in Lino da Silva's kinetic scheme in the sake of completeness,
- The use of the Harmonic Oscillator model for the vibrational partition function was assessed in comparison with the analytical calculation. The impact of the Harmonic Oscillator is negligible for the applications in this work, but could have greater impact at higher temperatures,
- The spontaneous emission modeling has been greatly improved from the previous approaches and led to non-negligible differences on the final results of the simulation,
- The vibrational redistribution method applied has proven to produce differences in the excited electronic states of molecules with later impact in the radiated power of the gas.

After modifying the kinetic models and simulating the shock tube flows we have reached the following two main conclusions:

- The results for a low shock wave speed are in reasonable agreement with the experimental data. This is not unexpected, since at least Gökçen's kinetic scheme was already used to successfully land the Huygens probe in Titan,
- The results for a high shock wave speed are not satisfactory in magnitude but the behavior exhibited are reasonable time-wise.

We have also stated that further improvements should be made to the kinetic modeling, namely the inclusion in the kinetics of dissociation of excited electronic states of N_2 and a physically consistent model for the vibrational redistribution. We hope that these changes will provide a better agreement than the one presented in this thesis and we intend to implement them in the future.

A Some aerodynamics derivations

This section we will derive some relations that are presented in chapter 2.

A.1 Mass conservation

Mass conservation is enforced on a species-by-species basis with a conservation equation for each species:

$$\frac{d\rho c_i}{dt} = \dot{\omega}_i.$$

The total derivative of the mass fraction c_i can be separated in it's temporal and convective parts,

$$\frac{\partial(\rho c_i)}{\partial t} + \boldsymbol{\nabla} \cdot (\rho \boldsymbol{u} c_i) = \dot{\omega}_i.$$

Neglecting the convective term we arrive at the formulation,

$$\frac{\partial c_i}{\partial t} = \frac{\dot{\omega}_i}{\rho}.$$

A.2 Energy conservation

Energy conservation is enforced through the usual equation

$$\frac{d\rho E}{dt} = \dot{\Omega}.$$

The internal energy E in an ideal gas is given by $E = C_v T$. The heat capacity C_v in a mixture of gases has contributions of every species present in the gas weighted by their relative mass fraction,

$$C_v = \sum_i c_i C_{v,i}.$$

Expanding the total time derivative of the conservation equation, by neglecting the convective term and inputting the definitions of internal energy and heat capacity we get

$$\rho C_v \frac{\partial T}{\partial t} + \rho T \frac{\partial}{\partial t}\left(\sum_i c_i C_{v,i}\right) = \dot{\Omega}.$$

By taking the derivative in time inside the summation on the second term of the LHS and rearranging the terms

$$\rho C_v \frac{\partial T}{\partial t} + \left(\sum_i \dot{\omega}_i C_{v,i} T\right) = \dot{\Omega}.$$

We can recognize the term $C_{v,i}T$ as the internal energy of species i which we denote by ϵ_i. We solve the equation in order to the temperature derivative:

$$\frac{\partial T}{\partial t} = \frac{1}{\rho C_v}\left(\dot{\Omega} - \sum_i \dot{\omega}_i \epsilon_i\right).$$

B Kinetic Database

This chapter introduces and explains how the kinetic scheme databases are used in this report. Firstly, we present Gökçen kinetics and it's evolution to a vibrational state specific model. Then we present Lino da Silva the updated kinetics. Finally, we present Magin's model and the spontaneous emission results of the equivalent Einstein coefficients. Finally, the FHO model used to model $N_2(X, v)$ VT and VD processes is briefly discussed.

B.1 Gökçen kinetics

B.1.1 Gökçen original kinetics or Gökçen Boltzmann

The original Gökçen kinetic is detailed in tables 2 taken from [5]. It contains 21 species and 37 reactions. Some reactions are defined using a generic collisional partner species: M_1 stands for all species, M_2 for molecules only, and M_3 for atoms only.

B.1.2 First modification to Gökçen kinetics or Gökçen Ess

The first modification of Gökçen kinetics is to accommodate electronic state specific kinetics. From table 2, every reaction that contains N_2 or CN is considered to have $N_2(X)$ and CN(X) instead. Magin Collisional-Radiative model is also added to expand Gökçen kinetics to include electronic excitation. Reactions 19 and 20 of Magin kinetics are not added at this stage because they are vibrational state specific, Spontaneous emission is given by the 9th order polynomials given in B.4 and explained in 3.3. Magin model is detailed in B.3.

B.1.3 Second modification to Gökçen kinetics or Gökçen Vss

The second modification to Gökçen kinetics introduces vibrational state specific kinetics. Reactions 19 and 20 of Magin are now added. Reactions included in Gökçen 1st modification are expanded as detailed in subsection 3.4.2, except reactions 1 and 2 which are given by the Forced Harmonic Oscillator Model further detailed in B.5. A total of 6 reactions are expanded from table 2, reactions 17, 20, 22, 26, 28 and 37. Vibrational excitation is also included through the addition of the FHO model.

Table 2: Gokcen's kinetic scheme. Taken from [5].

Number	Reaction	A (m^3/mol/s)	n	θ (K)
1	$N_2 + M_2 \rightleftarrows N + N + M_2$	7.00×10^{15}	−1.60	113200
2	$N_2 + M_3 \rightleftarrows N + N + M_3$	3.00×10^{16}	−1.60	113200
3	$N_2 + E^- \rightleftarrows N + N + E^-$	3.00×10^{18}	−1.60	113200
4	$CH_4 + M_1 \rightleftarrows CH_3 + H + M_1$	4.70×10^{41}	−8.20	59200
5	$CH_3 + M_1 \rightleftarrows CH_2 + H + M_1$	1.02×10^{10}	0.00	45600
6	$CH_3 + M_1 \rightleftarrows CH + H_2 + M_1$	5.00×10^{9}	0.00	42800
7	$CH_2 + M_1 \rightleftarrows CH + H + M_1$	4.00×10^{9}	0.00	41800
8	$CH_2 + M_1 \rightleftarrows C + H_2 + M_1$	1.30×10^{8}	0.00	29700
9	$CH + M_1 \rightleftarrows C + H + M_1$	1.90×10^{8}	0.00	33700
10	$C_2 + M_1 \rightleftarrows C + C + M_1$	1.50×10^{10}	0.00	71600
11	$H_2 + M_1 \rightleftarrows H + H + M_1$	2.23×10^{8}	0.00	48350
12	$CN + M_1 \rightleftarrows C + N + M_1$	2.53×10^{8}	0.00	71000
13	$NH + M_1 \rightleftarrows N + H + M_1$	1.80×10^{8}	0.00	37600
14	$HCN + M_1 \rightleftarrows CN + H + M_1$	3.57×10^{20}	0.00	62840
15	$CH_3 + N \rightleftarrows HCN + H + H$	7.00×10^{7}	0.00	0
16	$CH_3 + H \rightleftarrows CH_2 + H_2$	6.03×10^{7}	−2.60	7600
17	$CH_2 + N_2 \rightleftarrows HCN + NH$	4.82×10^{6}	0.00	18000
18	$CH_2 + N \rightleftarrows HCN + H$	5.00×10^{7}	0.00	0
19	$CH_2 + H \rightleftarrows CH + H_2$	6.03×10^{6}	0.00	− 900
20	$CH + N_2 \rightleftarrows HCN + N$	4.40×10^{6}	0.00	11060
21	$CH + C \rightleftarrows C_2 + H$	2.00×10^{8}	0.00	0
22	$C_2 + N_2 \rightleftarrows CN + CN$	1.50×10^{7}	0.00	21000
23	$CN + H_2 \rightleftarrows HCN + H$	2.95×10^{-1}	0.00	1130
24	$CN + C \rightleftarrows C_2 + N$	5.00×10^{7}	0.00	13000
25	$N + H_2 \rightleftarrows NH + H$	1.60×10^{8}	0.00	12650
26	$C + N_2 \rightleftarrows CN + N$	5.24×10^{7}	0.00	22600
27	$C + H_2 \rightleftarrows CH + H$	4.00×10^{8}	0.00	11700
28	$H + N_2 \rightleftarrows NH + N$	3.00×10^{6}	0.00	71400
29	$H + CH_4 \rightleftarrows CH_3 + H_2$	1.32×10^{-2}	0.00	4045
30	$N + N \rightleftarrows {N_2}^+ + E^-$	4.40×10^{1}	0.50	67500
31	$C + N \rightleftarrows CN^+ + E^-$	1.00×10^{9}	3.00	164400
32	$N + E^- \rightleftarrows N^+ + E^- + E^-$	2.50×10^{28}	1.50	168600
33	$C + E^- \rightleftarrows C^+ + E^- + E^-$	3.70×10^{25}	1.50	130700
34	$H + E^- \rightleftarrows H^+ + E^- + E^-$	2.20×10^{24}	−3.82	157800
35	$Ar + E^- \rightleftarrows Ar^+ + E^- + E^-$	2.50×10^{28}	−3.00	181700
36	$CN^+ + N \rightleftarrows CN + N^+$	9.80×10^{6}	0.00	40700
37	$C^+ + N_2 \rightleftarrows {N_2}^+ + C$	1.11×10^{8}	−0.11	50000

Table 3: Gökçen first modification or Gökçen Ess. Other reactions from table 2 and not featured here are kept the same. Spontaneous emission is given in table 8.

Number	Reaction	A (m^3/mol/s)	n	θ (K)
1	$N_2(X) + M_2 \rightleftarrows N + N + M_2$	7.00×10^{15}	-1.60	113200
2	$N_2(X) + M_3 \rightleftarrows N + N + M_3$	3.00×10^{16}	-1.60	113200
3	$N_2(X) + E^- \rightleftarrows N + N + E^-$	3.00×10^{18}	-1.60	113200
12	$CN(X) + M_1 \rightleftarrows C + N + M_1$	2.53×10^{8}	0.00	71000
14	$HCN + M_1 \rightleftarrows CN(X) + H + M_1$	3.57×10^{20}	0.00	62840
17	$CH_2 + N_2(X) \rightleftarrows HCN + NH$	4.82×10^{6}	0.00	18000
20	$CH + N_2(X) \rightleftarrows HCN + N$	4.40×10^{6}	0.00	11060
22	$C_2 + N_2(X) \rightleftarrows CN(X) + CN(X)$	1.50×10^{7}	0.00	21000
23	$CN(X) + H_2 \rightleftarrows HCN + H$	2.95×10^{-1}	0.00	1130
24	$CN(X) + C \rightleftarrows C_2 + N$	5.00×10^{7}	0.00	13000
26	$C + N_2(X) \rightleftarrows CN(X) + N$	5.24×10^{7}	0.00	22600
28	$H + N_2(X) \rightleftarrows NH + N$	3.00×10^{6}	0.00	71400
36	$CN^+ + N \rightleftarrows CN(X) + N^+$	9.80×10^{6}	0.00	40700
37	$C^+ + N_2(X) \rightleftarrows {N_2}^+ + C$	1.11×10^{8}	-0.11	50000
38	$CN(X) + M_1 \rightleftarrows CN(A) + M_1$	1.50×10^{5}	0.50	13300
39	$CN(X) + M_1 \rightleftarrows CN(B) + M_1$	1.80×10^{5}	0.50	37000
40	$N_2(X) + M_1 \rightleftarrows N_2(A) + M_1$	1.00×10^{6}	-0.50	71610
41	$N_2(A) + M_1 \rightleftarrows N_2(B) + M_1$	1.20×10^{7}	0.00	13495
42	$N_2(C) + M_1 \rightleftarrows N_2(B) + M_1$	5.10×10^{7}	0.00	0
43	$CN(X) + E^- \rightleftarrows CN(A) + E^-$	6.00×10^{8}	0.50	13300
44	$CN(X) + E^- \rightleftarrows CN(B) + E^-$	6.30×10^{8}	0.50	37000
45	$N_2(X) + E^- \rightleftarrows N_2(A) + E^-$	2.40×10^{9}	0.10	71610
46	$N_2(X) + E^- \rightleftarrows N_2(B) + E^-$	2.80×10^{10}	-0.10	85740
47	$N_2(X) + E^- \rightleftarrows N_2(C) + E^-$	2.30×10^{9}	0.10	127900
48	$N_2(A) + E^- \rightleftarrows N_2(B) + E^-$	3.00×10^{9}	0.00	13495
49	$N_2(A) + N_2(A) \rightleftarrows N_2(X) + N_2(B)$	1.80×10^{8}	0.00	0
50	$N_2(A) + N_2(A) \rightleftarrows N_2(X) + N_2(C)$	9.00×10^{7}	0.00	0
51	$N_2(A) + CN(X) \rightleftarrows N_2(X) + CN(B)$	4.20×10^{6}	0.50	0

Table 4: Gökçen second modification or Gökçen Vss. Other reactions from table 3 and not featured here are kept the same. Spontaneous emission is given in table 8. An asterisk "$*$" in the last column means that the rates used have gone through the vibrational redistribution procedure detailed in section 3.4.2.

Number	Reaction	A (m^3/mol/s)	n	θ (K)	Model
1	$N_2(X, v_i) + M_2 \rightleftarrows N + N + M_3$	-	-	-	FHO
2	$N_2(X, v_i) + M_3 \rightleftarrows N + N + M_2$	-	-	-	FHO
3	$N_2(X, v_i) + E^- \rightleftarrows N + N + E^-$	-	-	-	Gökçen $*$
17	$CH_2 + N_2(X, v_i) \rightleftarrows HCN + NH$	-	-	-	Gökçen $*$
20	$CH + N_2(X, v_i) \rightleftarrows HCN + N$	-	-	-	Gökçen $*$
22	$C_2 + N_2(X, v_i) \rightleftarrows CN(X) + CN(X)$	-	-	-	Gökçen $*$
26	$C + N_2(X, v_i) \rightleftarrows CN(X) + N$	-	-	-	Gökçen $*$
28	$H + N_2(X, v_i) \rightleftarrows NH + N$	-	-	-	Gökçen $*$
37	$C^+ + N_2(X, v_i) \rightleftarrows {N_2}^+ + C$	-	-	-	Gökçen $*$
40	$N_2(X, v_i) + M_1 \rightleftarrows N_2(A) + M_1$	-	-	-	Magin $*$
45	$N_2(X, v_i) + E^- \rightleftarrows N_2(A) + E^-$	-	-	-	Magin $*$
46	$N_2(X, v_i) + E^- \rightleftarrows N_2(B) + E^-$	-	-	-	Magin $*$
47	$N_2(X, v_i) + E^- \rightleftarrows N_2(C) + E^-$	-	-	-	Magin $*$
49	$N_2(A) + N_2(A) \rightleftarrows N_2(X, v_i) + N_2(B)$	-	-	-	Magin $*$
50	$N_2(A) + N_2(A) \rightleftarrows N_2(X, v_i) + N_2(C)$	-	-	-	Magin $*$
51	$N_2(A) + CN(X) \rightleftarrows N_2(X, v_i) + CN(B)$	-	-	-	Magin $*$
52	$CN(X) + N_2(X, 4) \rightleftarrows CN(A) + N_2(X, 0)$	6.00×10^7	0.00	0	Magin
53	$CN(X) + N_2(X, 11) \rightleftarrows CN(B) + N_2(X, 0)$	6.00×10^7	0.00	0	Magin
54	$N_2(X, v_i) + M_3 \rightleftarrows N_2(X, v_f) + M_3$	-	-	-	FHO
55	$N_2(X, v_i) + M_2 \rightleftarrows N_2(X, v_f) + M_2$	-	-	-	FHO

B.2 Lino da Silva kinetics

B.2.1 Lino da Silva original kinetics or Lino da Silva Boltzmann

Lino da Silva kinetics is in table 5 as taken from [9]. Lino da Silva is meant to be an update from Gokcen. It features 24 species and 45 reactions. The definitions of generic collisional partners in B.1.1 apply to this kinetic. Reaction 45 of table 5, N_2 dissociation by electronic impact, was calculated as in section 3.3 and is a part of this work.

B.2.2 First modification to Lino da Silva kinetics or Lino da Silva Ess

Lino da Silva kinetics was modified to accommodate electronic state specific kinetics. Reactions that contain N_2 or CN are considered to have N_2(X) and CN(X) instead. Magin Collisional-Radiative model is also added to expand Lino da Silva kinetics to include electronic excitation, except reactions 19 and 20 which are vibrational state specific. Magin model is detailed in B.3. Spontaneous emission is added through the rates computed as explained in subsection 3.3. The results of this computation are shown in B.4.

B.2.3 Second modification to Lino da Silva kinetics or Lino da Silva Vss

The second modification of Lino da Silva kinetics is to accommodate vibrational state specific kinetics. Reactions 19 and 20 from Magin are added. Reactions included in Lino da Silva 1st modification are expanded as detailed in subsection 3.4.2, except reactions 1 and 2 which are given by the Forced Harmonic Oscillator Model further detailed in B.5. A total of 10 reactions are expanded from table 5, reactions 16, 19, 21, 25, 27. 40 and 42 to 45. Vibrational excitation is also included through the addition of the FHO model.

Table 5: Lino da Silva original kinetic scheme reactions. Taken from [9].

Number	Reaction	A (m^3/mol/s)	n	θ (K)
1	$N_2 + M_2 \rightleftarrows N + N + M_2$	1.72×10^{12}	-0.89	111700
2	$N_2 + M_3 \rightleftarrows N + N + M_3$	1.21×10^{13}	-0.89	111700
3	$CH_4 + M_1 \rightleftarrows CH_3 + H + M_1$	1.06×10^{16}	-1.46	49990
4	$CH_3 + M_1 \rightleftarrows CH_2 + H + M_1$	2.82×10^{8}	0.00	42460
5	$CH_3 + M_1 \rightleftarrows CH + H_2 + M_1$	5.00×10^{9}	0.00	42800
6	$CH_2 + M_1 \rightleftarrows CH + H + M_1$	4.00×10^{9}	0.00	41800
7	$CH_2 + M_1 \rightleftarrows C + H_2 + M_1$	1.30×10^{8}	0.00	29700
8	$CH + M_1 \rightleftarrows C + H + M_1$	1.90×10^{8}	0.00	33700
9	$C_2 + M_1 \rightleftarrows C + C + M_1$	3.72×10^{8}	0.00	69800
10	$H_2 + M_1 \rightleftarrows H + H + M_1$	2.23×10^{8}	0.00	48350
11	$CN + M_1 \rightleftarrows C + N + M_1$	2.53×10^{8}	0.00	71000
12	$NH + M_1 \rightleftarrows N + H + M_1$	1.80×10^{8}	0.00	37600
13	$HCN + M_1 \rightleftarrows CN + H + M_1$	3.57×10^{20}	-2.60	62845
14	$CH_3 + N \rightleftarrows HCN + H + H$	7.00×10^{7}	0.00	0
15	$CH_3 + H \rightleftarrows CH_2 + H_2$	6.03×10^{7}	0.00	7600
16	$CH_2 + N_2 \rightleftarrows HCN + NH$	4.82×10^{6}	0.00	18000
17	$CH_2 + N \rightleftarrows HCN + H$	5.00×10^{7}	0.00	0
18	$CH_2 + H \rightleftarrows CH + H_2$	4.21×10^{2}	-0.09	-1560
19	$CH + N_2 \rightleftarrows HCN + N$	4.40×10^{6}	0.00	11060
20	$CH + C \rightleftarrows C_2 + H$	2.00×10^{8}	0.00	0
21	$C_2 + N_2 \rightleftarrows CN + CN$	1.50×10^{7}	0.00	21000
22	$CN + H_2 \rightleftarrows HCN + H$	2.95×10^{-1}	0.00	1130
23	$CN + C \rightleftarrows C_2 + N$	3.00×10^{8}	0.00	18040
24	$N + H_2 \rightleftarrows NH + H$	1.60×10^{8}	0.00	12650
25	$C + N_2 \rightleftarrows CH + N$	5.24×10^{7}	0.00	22600
26	$C + H_2 \rightleftarrows CH + H$	4.00×10^{8}	0.00	11700
27	$H + N_2 \rightleftarrows NH + N$	3.00×10^{6}	-0.50	71400
28	$H + H \rightleftarrows {H_2}^+ + E^-$	1.13×10^{9}	-0.06	129060
29	$C + H \rightleftarrows CH^+ + E^-$	9.95×10^{5}	0.52	84830
30	$C + N \rightleftarrows CN^+ + E^-$	3.80×10^{6}	0.33	74810
31	$N + H \rightleftarrows NH^+ + E^-$	2.99×10^{8}	-0.06	118760
32	$N + N \rightleftarrows {N_2}^+ + E^-$	2.13×10^{4}	0.48	69190
33	$N + E^- \rightleftarrows N^+ + E^- + E^-$	1.67×10^{7}	0.59	143220
34	$C + E^- \rightleftarrows C^+ + E^- + E^-$	1.24×10^{9}	0.28	142700
35	$H + E^- \rightleftarrows H^+ + E^- + E^-$	1.36×10^{7}	0.18	169000
36	$Ar + E^- \rightleftarrows Ar^+ + E^- + E^-$	5.52×10^{7}	0.58	186210
37	$H_2 + E^- \rightleftarrows {H_2}^+ + E^- + E^-$	4.05×10^{7}	0.52	180767
38	$CH + E^- \rightleftarrows CH^+ + E^- + E^-$	1.15×10^{6}	0.87	123430
39	$NH + E^- \rightleftarrows NH^+ + E^- + E^-$	2.39×10^{7}	0.59	172430
40	$N_2 + E^- \rightleftarrows {N_2}^+ + E^- + E^-$	5.92×10^{5}	0.92	178630
41	${N_2}^+ + E^- \rightleftarrows N^+ + N + E^-$	7.47×10^{5}	0.84	80600
42	$C^+ + N_2 \rightleftarrows {N_2}^+ + C$	1.01×10^{5}	0.60	53830
43	$C^+ + N_2 \rightleftarrows CN^+ + N$	1.32×10^{6}	0.33	51430
44	$C^+ + N_2 \rightleftarrows N^+ + CN$	8.93×10^{7}	-0.14	65260
45	$N_2 + E^- \rightleftarrows N + N + E^-$	2.86×10^{6}	0.78	125248

Table 6: First modification of Lino da Silva or Lino da Silva Ess. Other reactions from table 5 and not featured here stay the same. Spontaneous emission is given in table 10.

Number	Reaction	A (m^3/mol/s)	n	θ (K)
1	$N_2(X) + M_2 \rightleftarrows N + N + M_2$	1.72×10^{12}	-0.89	111700
2	$N_2(X) + M_3 \rightleftarrows N + N + M_3$	1.21×10^{13}	-0.89	111700
11	$CN(X) + M_1 \rightleftarrows C + N + M_1$	2.53×10^{8}	0.00	71000
13	$HCN + M_1 \rightleftarrows CN(X) + H + M_1$	3.57×10^{20}	-2.60	62845
16	$CH_2 + N_2(X) \rightleftarrows HCN + NH$	4.82×10^{6}	0.00	18000
19	$CH + N_2(X) \rightleftarrows HCN + N$	4.40×10^{6}	0.00	11060
21	$C_2 + N_2(X) \rightleftarrows CN(X) + CN(X)$	1.50×10^{7}	0.00	21000
22	$CN(X) + H_2 \rightleftarrows HCN + H$	2.95×10^{-1}	0.00	1130
23	$CN(X) + C \rightleftarrows C_2 + N$	3.00×10^{8}	0.00	18040
25	$C + N_2(X) \rightleftarrows CH + N$	5.24×10^{7}	0.00	22600
27	$H + N_2(X) \rightleftarrows NH + N$	3.00×10^{6}	-0.50	71400
40	$N_2(X) + E^- \rightleftarrows {N_2}^+ + E^- + E^-$	5.92×10^{5}	0.92	178630
42	$C^+ + N_2(X) \rightleftarrows {N_2}^+ + C$	1.01×10^{5}	0.60	53830
43	$C^+ + N_2(X) \rightleftarrows CN^+ + N$	1.32×10^{6}	0.33	51430
44	$C^+ + N_2(X) \rightleftarrows N^+ + CN(X)$	8.93×10^{7}	-0.14	65260
45	$N_2(X) + E^- \rightleftarrows N + N + E^-$	2.86×10^{6}	0.78	125248
46	$CN(X) + M_1 \rightleftarrows CN(A) + M_1$	1.50×10^{5}	0.50	13300
47	$CN(X) + M_1 \rightleftarrows CN(B) + M_1$	1.80×10^{5}	0.50	37000
48	$N_2(X) + M_1 \rightleftarrows N_2(A) + M_1$	1.00×10^{6}	-0.50	71610
49	$N_2(A) + M_1 \rightleftarrows N_2(B) + M_1$	1.20×10^{7}	0.00	13495
50	$N_2(C) + M_1 \rightleftarrows N_2(B) + M_1$	5.10×10^{7}	0.00	0
51	$CN(X) + E^- \rightleftarrows CN(A) + E^-$	6.00×10^{8}	0.50	13300
52	$CN(X) + E^- \rightleftarrows CN(B) + E^-$	6.30×10^{8}	0.50	37000
53	$N_2(X) + E^- \rightleftarrows N_2(A) + E^-$	2.40×10^{9}	0.10	71610
56	$N_2(X) + E^- \rightleftarrows N_2(B) + E^-$	2.80×10^{10}	-0.10	85740
57	$N_2(X) + E^- \rightleftarrows N_2(C) + E^-$	2.30×10^{9}	0.10	127900
58	$N_2(A) + E^- \rightleftarrows N_2(B) + E^-$	3.00×10^{9}	0.00	13495
59	$N_2(A) + N_2(A) \rightleftarrows N_2(X) + N_2(B)$	1.80×10^{8}	0.00	0
60	$N_2(A) + N_2(A) \rightleftarrows N_2(X) + N_2(C)$	9.00×10^{7}	0.00	0
61	$N_2(A) + CN(X) \rightleftarrows N_2(X) + CN(B)$	4.20×10^{6}	0.50	0

Table 7: Lino da Silva second modification or Lino da Silva Vss. Other reactions from table 6 and not featured here are kept the same. Spontaneous emission is given in table 10. An asterisk "$*$" in the last column means that the rates used have gone through the vibrational redistribution procedure detailed in section 3.4.2.

Number	Reaction	A (m^3/mol/s)	n	θ (K)	Model
1	$N_2(X, v_i) + M_2 \rightleftarrows N + N + M_3$	-	-	-	FHO
2	$N_2(X, v_i) + M_3 \rightleftarrows N + N + M_2$	-	-	-	FHO
16	$CH_2 + N_2(X, v_i) \rightleftarrows HCN + NH$	-	-	-	Lino da Silva $*$
19	$CH + N_2(X, v_i) \rightleftarrows HCN + N$	-	-	-	Lino da Silva $*$
21	$C_2 + N_2(X, v_i) \rightleftarrows CN(X) + CN(X)$	-	-	-	Lino da Silva $*$
25	$C + N_2(X, v_i) \rightleftarrows CH + N$	-	-	-	Lino da Silva $*$
27	$H + N_2(X, v_i) \rightleftarrows NH + N$	-	-	-	Lino da Silva $*$
40	$N_2(X, v_i) + E^- \rightleftarrows {N_2}^+ + E^- + E^-$	-	-	-	Lino da Silva $*$
42	$C^+ + N_2(X, v_i) \rightleftarrows {N_2}^+ + C$	-	-	-	Lino da Silva $*$
43	$C^+ + N_2(X, v_i) \rightleftarrows CN^+ + N$	-	-	-	Lino da Silva $*$
44	$C^+ + N_2(X, v_i) \rightleftarrows N^+ + CN(X)$	-	-	-	Lino da Silva $*$
45	$N_2(X, v_i) + E^- \rightleftarrows N + N + E^-$	-	-	-	Lino da Silva $*$
46	$N_2(X, v_i) + M_1 \rightleftarrows N_2(A) + M_1$	-	-	-	Magin $*$
51	$N_2(X, v_i) + E^- \rightleftarrows N_2(A) + E^-$	-	-	-	Magin $*$
52	$N_2(X, v_i) + E^- \rightleftarrows N_2(B) + E^-$	-	-	-	Magin $*$
53	$N_2(X, v_i) + E^- \rightleftarrows N_2(C) + E^-$	-	-	-	Magin $*$
55	$N_2(A) + N_2(A) \rightleftarrows N_2(X, v_i) + N_2(B)$	-	-	-	Magin $*$
56	$N_2(A) + N_2(A) \rightleftarrows N_2(X, v_i) + N_2(C)$	-	-	-	Magin $*$
57	$N_2(A) + CN(X) \rightleftarrows N_2(X, v_i) + CN(B)$	-	-	-	Magin $*$
58	$CN(X) + N_2(X, 4) \rightleftarrows CN(A) + N_2(X, 0)$	6.00×10^7	0.00	0	Magin
59	$CN(X) + N_2(X, 11) \rightleftarrows CN(B) + N_2(X, 0)$	6.00×10^7	0.00	0	Magin
60	$N_2(X, v_i) + M_3 \rightleftarrows N_2(X, v_f) + M_3$	-	-	-	FHO
61	$N_2(X, v_i) + M_2 \rightleftarrows N_2(X, v_f) + M_2$	-	-	-	FHO

B.3 Magin CR model

Tables 8 and 9 contain Magin CR model as taken from [6], which is used coupled with Gökçen or Lino da Silva kinetics on their first and second modifications. In table 9, the generic collisional partner M is used. Magin kinetic specifies that this collisional partner is N_2. In this case, we treat this generic collisional partner as any specie which is not an electron, as reactions 5 to 8 are the same as reactions 10 to 12 and 15 but with different collisional partners. This approximation is to account for other collisional partners which are present in the flow and might contribute to electronic excitation of N_2 and CN. Rates 7, 12 to 14 and 16 to 18 were expanded as explained in subsection 3.4.2. The spontaneous emission rates in table 8 are not used but kept here for completeness.

Table 8: Magin CR model reactions 1 to 4. Taken from [6].

Number	Reaction	Forward Rate (s^{-1})
1	$CN(A) \longrightarrow CN(X)$	6.49×10^4
2	$CN(B) \longrightarrow CN(X)$	1.52×10^7
3	$N_2(B) \longrightarrow N_2(A)$	1.42×10^5
4	$N_2(C) \longrightarrow N_2(B)$	2.73×10^7

Table 9: Magin CR model, reactions 5 to 20. Taken from [6].

Number	Reaction	A (m^3/mol/s)	n	θ (K)
5	$CN(X) + M \rightleftarrows CN(A) + M$	1.50×10^5	0.50	13300
6	$CN(X) + M \rightleftarrows CN(B) + M$	1.80×10^5	0.50	37000
7	$N_2(X) + M \rightleftarrows N_2(A) + M$	1.00×10^6	−0.50	71610
8	$N_2(A) + M \rightleftarrows N_2(B) + M$	1.20×10^7	0.00	13495
9	$N_2(C) + M \rightleftarrows N_2(B) + M$	5.10×10^7	0.00	0
10	$CN(X) + E^- \rightleftarrows CN(A) + E^-$	6.00×10^8	0.50	13300
11	$CN(X) + E^- \rightleftarrows CN(B) + E^-$	6.30×10^8	0.50	37000
12	$N_2(X) + E^- \rightleftarrows N_2(A) + E^-$	2.40×10^9	0.10	71610
13	$N_2(X) + E^- \rightleftarrows N_2(B) + E^-$	2.80×10^{10}	−0.10	85740
14	$N_2(X) + E^- \rightleftarrows N_2(C) + E^-$	2.30×10^9	0.10	127900
15	$N_2(A) + E^- \rightleftarrows N_2(B) + E^-$	3.00×10^9	0.00	13495
16	$N_2(A) + N_2(A) \rightleftarrows N_2(X) + N_2(B)$	1.80×10^8	0.00	0
17	$N_2(A) + N_2(A) \rightleftarrows N_2(X) + N_2(C)$	9.00×10^7	0.00	0
18	$N_2(A) + CN(X) \rightleftarrows N_2(X) + CN(B)$	4.20×10^6	0.50	0
19	$CN(X) + N_2(X, 4) \rightleftarrows CN(A) + N_2(X, 0)$	6.00×10^7	0.00	0
20	$CN(X) + N_2(X, 11) \rightleftarrows CN(B) + N_2(X, 0)$	6.00×10^7	0.00	0

B.4 Calculated rates of spontaneous emission

In table 10 the fit results from the equivalent Einstein coefficients are shown. For convenience, the fitted function is also placed here

$$A^*(\tilde{T}) = \exp\left(\sum_{k=-3}^{4} c_k \tilde{T}^k + c_5 \log \tilde{T}\right),$$

where $\tilde{T} = T/1000$. Data for the Einstein coefficients was taken from [16] for N_2 transitions and from [14] for CN transitions.

Table 10: Fitted rates for equivalent Einstein coefficients.

	$N_2(C \longrightarrow B)$	$N_2(B \longrightarrow A)$	$CN(B \longrightarrow X)$	$CN(A \longrightarrow X)$	$CN(B \longrightarrow A)$
a_{-3}	-8.683×10^{-3}	1.003×10^{-4}	4.627×10^{-4}	4.043×10^{-3}	4.028×10^{-3}
a_{-2}	7.955×10^{-2}	-1.241×10^{-3}	-8.561×10^{-3}	-7.337×10^{-2}	-6.974×10^{-2}
a_{-1}	-3.039×10^{-1}	5.205×10^{-3}	5.504×10^{-2}	4.463×10^{-1}	3.772×10^{-1}
a_0	1.733×10^{1}	1.121×10^{1}	1.654×10^{1}	1.095×10^{1}	1.096×10^{1}
a_1	1.236×10^{-2}	-3.657×10^{-4}	-1.690×10^{-2}	-1.448×10^{-2}	5.082×10^{-2}
a_2	-1.761×10^{-4}	4.088×10^{-6}	2.571×10^{-4}	9.762×10^{-5}	-1.185×10^{-3}
a_3	1.465×10^{-6}	7.935×10^{-8}	-2.034×10^{-6}	-1.285×10^{-7}	1.201×10^{-5}
a_4	-4.914×10^{-9}	-4.980×10^{-10}	6.393×10^{-9}	-1.277×10^{-9}	-4.476×10^{-8}
a_5	-1.883×10^{-1}	2.839×10^{-3}	5.312×10^{-2}	3.467×10^{-1}	1.993×10^{-1}

B.5 Forced Harmonic Oscillator

The forced harmonic oscillator (FHO) model is a Vss model with a purpose to model vibrational excitation and vibrational excited states dissociation. As $N_2(X)$ is the only electronic level which is also Vss. With 61 vibrational levels, it becomes impossible to list all reactions that are applied to our kinetic scheme using FHO. The type of reactions included are

- Dissociation by atomic impact $N_2(X, v_i) + M_3 \rightleftarrows 2\,N + M_3$. N is always considered to be in the ground state with $v_i = 0$ to 60.
- Dissociation by molecular impact $N_2(X, v_i) + M_2 \rightleftarrows 2\,N + M_2$. Same restrictions as mono-nucleus impact.
- Vibrational excitation by atomic impact $N_2(X, v_i) + M_3 \rightleftarrows N_2(X, v_f) + M_3$, in which $v_i < v_f$.
- Vibrational excitation by molecular impact $N_2(X, v_i) + M_2 \rightleftarrows N_2(X, v_f) + M_2$, in which $v_i < v_f$.

The details on how these rates are obtained should be consulted in [3]. More details on the original model can be seen in [19, 20].

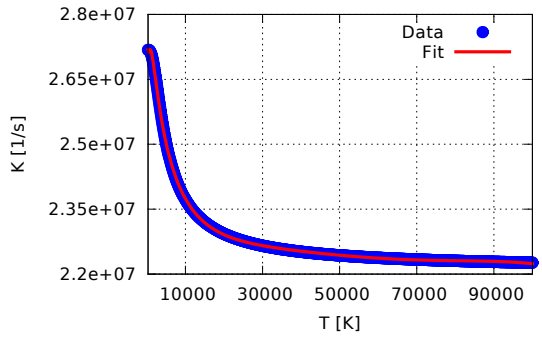

(a) Fit for equivalent Einstein coefficient of $N_2(C \longrightarrow B)$.

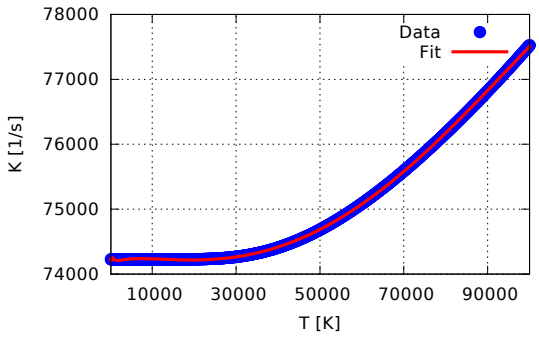

(b) Fit for equivalent Einstein coefficient of $N_2(B \longrightarrow A)$.

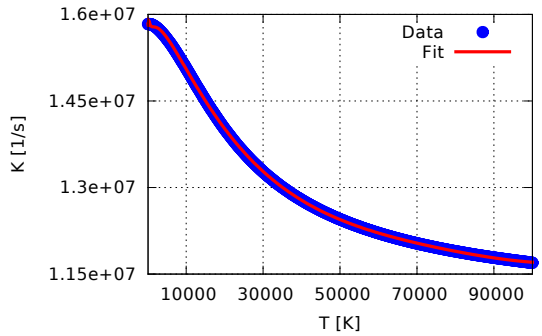

(c) Fit for equivalent Einstein coefficient of $CN(B \longrightarrow X)$.

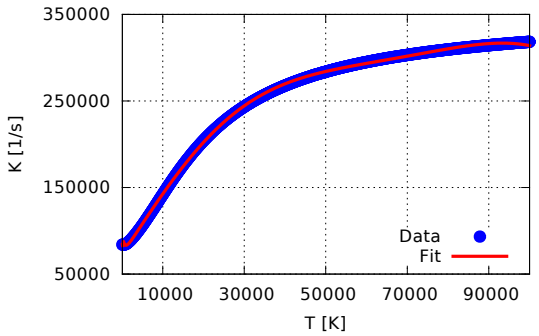

(d) Fit for equivalent Einstein coefficient of $CN(B \longrightarrow A)$.

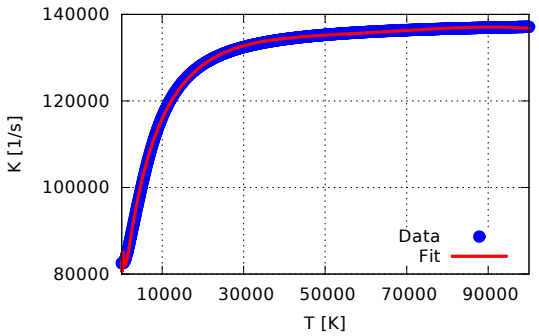

(e) Fit for equivalent Einstein coefficient of $CN(A \longrightarrow X)$.

Figure 24: Fits for the equivalent Einstein coefficients.

References

[1] J.D. Anderson Jr., *Hypersonic And High Temperature Gas Dynamics Second Edition*, AIAA Education Series, AIAA Reston, Virginia, 2006.

[2] B. Lopez, M. Lino da Silva, V. Guerra, J. Loureiro, *Coupled Hydrodynamic/State-Specific High-Temperature Modeling of Nitrogen Vibrational Excitation and Dissociation*, 44th AIAA Thermophysics Conference, June, AIAA Paper, 2013.

[3] M. Lino da Silva, V. Guerra, J. Loureiro, *State-Resolved Dissociation Rates For Extremely Non-Equilibrium Atmospheric Entries*, Journal of Thermophysics and Heat Transfer AIAA, V.21, N.1, 2007.

[4] G.G. Chernyi, S.A. Losev, S.O. Macheret, B. V. Potapkin, *Physical and Chemical Processes in Gas Dynamics: Cross Sections and Rate Contants* Volume I, Progress in Astronautics and Aeronautics, Volume 196, AIAA Reston, Virginia, 2002.

[5] T. Gökçen, N_2-CH_4-Ar *Chemical Kinetic Model for Simulations of Titan Atmospheric Entry*, Journal of Thermophysics and Heat Transfer AIAA, V21, N.1, 2007.

[6] T.E. Magin, L. Caillaut, A. Bourdon, C.O. Laux, *Non-Equilibrium Radiative Heat Flux Modeling For Huygens Entry Probe*, Journal of Geophysical Research, V.111, 2006.

[7] A. Brandis, *Experimental Study And Modeling of Non-Equilibrium Radiations During Titan and Martian Entry*, PhD Thesis, University of Queensland, 2009.

[8] M. Lino da Silva, D. Tsyhanou, V. Guerra, J. Loureiro, *Simulation of* N_2-CH_4 *Shocked Flows Using a Multiquantum State-to-State Model*, Technical Report, 2011.

[9] M. Lino da Silva, D. Tsyhanou, V. Guerra, J. Loureiro, *A Physically-Consistent Chemical Dataset for the Simulation of* N_2-CH_4 *Shocked Flows Up to* $T = 100000$ *K*, Technical Report, 2011.

[10] B.J. McBride, S. Gordon, M.A. Reno, *Coefficients for Calculating Thermodynamic and Transport Properties of Individual Species*, NASA Technical Memorandum, 1993.

[11] K.P. Huber, G. Herzberg, *Molecular Spectra and Molecular Structure*, Van Nostrand Reinhold Company, V. IV - Constants of Diatomic Molecules, 1979.

[12] F. Roux, F. Michaud, *Investigation of The Rovibrational Levels of the B3P State of* $^{14}N_2$ *Molecule Above the Dissociation Limit of* $N(^4S) + N(^4S)$ *by Fourier Transform Spectrometry*, Canadian Journal of Physics, V.68, p1257, 1990.

[13] R.R. Laher, F.R. Gilmore, *Improved Fits for the Vibrational and Rotational Constants of Many States of Nitrogen and Oxygen*, Journal of Physical and Chemical Reference Data, V.20, N.4, p685-712, 1991.

[14] M. Lino da Silva, *Simulation des Propértés Radiatives du Plasma Entourant un Vehicle Planétaire á Vitesse Hypersonique*, PhD Thesis, Universite d'Orleans, 2004.

[15] C.V.V. Prasad, P.F. Bernath *Fourier Transform Jet-Emission Spectroscopy of the* $A^2\Pi_j - X^2\Sigma^+$ *Transition of CN*, Journal of Molecular Spectroscopy, V.156, p327-340, 1992.

[16] O. Laux, *Optical Diagnostics and Radiative Emission of Air Plasmas* PhD Thesis, Stanford University, 1993.

[17] V. Laporta, D.A. Little, R. Celiberto, J. Tennyson, *ELectron-Impact Resonant Vibrational Excitation and Dissociation Processes Involving Vibrationally Excited* N_2 *Molecules*, Plasma Sources Science and Technology, V.23, 2014.

[18] E.C. Zipf, R.W. MacLaughlin, *On the Dissociation By Electron Impact and by E.U.V Photo-Absorption* Planetary and Space Science, V.26, Issue 5, p449-462, 1978.

[19] A. Zelechow, D. Rapp, T.E. Sharp, *Vibrational-Vibrational Translational Transfer Between Two Diatomic Molecules*, Journal of Chemical Physics, V.49, N.1, 1968.

[20] D. Rapp, T.E. Sharp, *Vibrational Energy Transfer in Molecular Collisions Involving Large Transition Probabilities* Journal of Chemical Physics, V.38, N.11, 1963.

[21] P. Teulet, J.P. Sarrette, A.M. Gomes, *Calculation of Electron Impact Inelastic Cross Sections and Rate Coefficients for Diatomic Molecules, Application to Air Molecules* Journal of Quantitative Spectroscopy and Radiative Transfer, V.62, p549-569, 1999.

[22] P. N. Brown, G. D. Byrne, A. C. Hindmarsh, *VODE: A Variable-coefficient ODE Solver*, SIAM J. Sci. Stat. Comput., V.10, No.5, p1038-1051, 1989.

[23] P.A. Gnoffo, *A Perspective on Computational Aerothermodynamics at NASA*, 16th Australasian Fluid Mechanics Conference, 2007.

[24] C. Park, R. L. Jaffe, H. Partridge, *Chemical-Kinetic Parameters of Hyperbolic Earth Entry*, Journal of Thermophysics and Heat Transfer AIAA, V.15, No.1, p76-90, 2001.

[25] A.W. Irwin, *The partition functions of JANAF polyatomic molecules that significantly affect the stellar atmospheric equation of state*, Astronomy & Astrophysics Supplement Series, V.74, p145-160, 1988.

[26] J. Annaloro, *Modèles collisionels-radiatifs appliqués aux situations d'entreée atmosphérique martienne et terrestre*, PhD Thesis, University of Rouen, 2013.

[27] M.W. Chase, C.A. Davies, J.R. Downey, D.J. Frurip, R.A. McDonald, A.N. Syverud, *JANAF Thermochemical Tables Third Edition*, Analytical Chemistry, V.62, N.10, 1990.